An Arp2/3-cPLA$_2$-NFκB axis acts as a Cell Shape Sensor to drive Homeostatic Migration of Dendritic Cells

Zahraa Alraies[1], Claudia A. Rivera[1], Maria-Graciela Delgado[1*], Doriane Sanséau[1*], Mathieu Maurin[1], Aline Yatim[1], Pablo Saez[2,3], Alice Williart[2], Matthieu Gratia[1], Nilushi S. De Silva[1], Aurélie Moreau[4], Benoit Albaud[1], Patricia Legoix[1], Hideki Nakano[5], Donald N Cook[5], Toby Lawrence[6,7], Nicolas Manel[1], Hélène D. Moreau[1], Guilherme P.F. Nader[2#], Matthieu Piel [2#†] and Ana-Maria Lennon-Duménil[1#†]

[1] Institut Curie, PSL University, Inserm U932, Immunity and Cancer, 75005 Paris, France

[2] Institut Curie, PSL Research University, CNRS UMR144; Paris, France

[3] Cell Communication and Migration Laboratory, Institute of Biochemistry and Molecular Cell Biology, Center for Experimental Medicine, University Medical Center Hamburg-Eppendorf, Hamburg, Germany

[4] INSERM, Nantes Université, CHU Nantes, Nantes Université, Centre de Recherche Translationnelle en Transplantation et Immunologie UMR1064, ITUN, Nantes, France

[5] Immunity, Inflammation, and Disease Laboratory, National Institute of Environmental Health Sciences (NIEHS), National Institutes of Health (NIH), Research Triangle Park, North Carolina, USA

[6] Centre d'Immunologie de Marseille-Luminy, Université Aix-Marseille, INSERM, CNRS, Marseille, France

[7] Centre for Inflammation Biology and Cancer Immunology, School of Immunology and Microbial Sciences, King's College London, UK

* These authors contributed equally to the experimental part of this work

# These authors jointly supervised this work

†Corresponding authors: ana-maria.lennon@curie.fr & matthieu.piel@curie.fr

Keywords: dendritic cells, cell migration, immune regulation, CCR7, cPLA$_2$, ARP2/3, Arpin, F-actin, nuclear ruler pathway, lymph node migration, transcriptional reprogramming, immune tolerance.

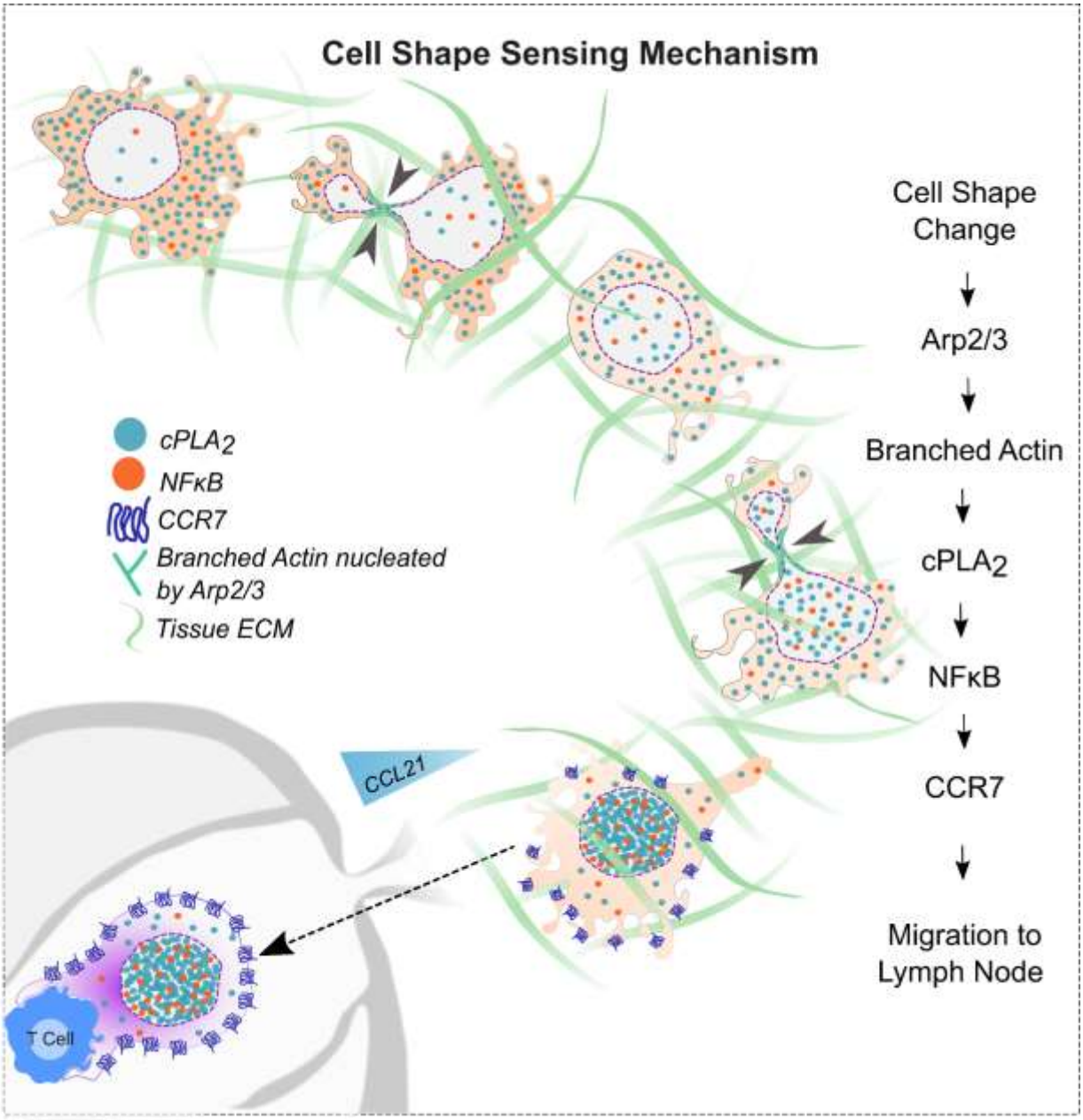

HIGHLIGHTS

- Dendritic cells express the lymph node guiding chemokine receptor CCR7 upon activation of a cell shape sensor.
- Cell shape sensing is driven by an ARP2/3-cPLA$_2$ signaling axis that activates NFκB upstream of CCR7 expression.
- Activation of this shape-sensitive axis reprograms dendritic cells towards a specific immunoregulatory phenotype, distinct from the one induced by microbes.
- Cell shape sensing might constitute the long sought-after signal that drives homeostatic dendritic cells migration for maintenance of tolerance to self.

Abstract

Dendritic cells (DCs) patrol tissues and migrate to lymph nodes for presentation of collected antigens to T cells. This process is needed to initiate immune responses against infectious agents as well as to maintain tolerance to tissue self-antigens at steady state. In both cases, DC migration to lymph nodes requires the upregulation of the chemokine receptor CCR7. It is well-known that upon infection, CCR7 expression is induced by microbial and inflammatory components released within the tissue environment. However, the environmental signals that trigger CCR7 expression and homeostatic DC migration to lymph nodes at steady state remain unidentified. Here we show that the changes in cell shape experienced by tissue patrolling DCs are sufficient to induce CCR7 expression at their surface and their migration to lymph nodes. Cell shape sensing requires ARP2/3-dependent activation of the lipid metabolism enzyme cytosolic phospholipase 2 ($cPLA_2$) acting upstream of NFκB. Activation of this shape-sensitive axis reprograms DCs towards a specific immunoregulatory phenotype that is distinct from the one induced by microbes and leads to T cell hypo-responsiveness. We propose that cell shape sensing might constitute the long sought-after signal that drives homeostatic DC migration to lymph nodes for maintenance of tolerance to self.

Introduction

The success of immune responses relies on the ability of immune cells to be at the right time at the right place. These cells circulate between peripheral tissues and/or lymphoid organs through blood and lymph vessels. Among lymphoid organs, lymph nodes are of major importance as this is where adaptive immune responses are initiated by dendritic cells (DCs) that transport antigens from peripheral tissues to present them to circulating T lymphocytes (1; 2; 3). DC migration and antigen presentation are essential to activate T cells and develop adaptive immune responses against infectious agents (2; 4; 5). However, DC migration to lymph nodes also occurs in the absence of infection and inflammation (a state of tissue called steady state). This process is referred to as homeostatic DC migration and is needed for presentation of self-antigens and maintenance of tolerance to self (6). Accordingly, disruption of homeostatic DC migration was shown to lead to autoimmunity (6).

To reach and enter lymph nodes, immune cells must upregulate the C-C chemokine receptor type 7 (CCR7) at their surface, which guides them along gradients of CCL21 or CCL19 chemokines (7) (8). The environmental signals that control the expression of CCR7 have therefore been intensively investigated. This led to the identification of different molecules such as Pathogen- and Danger-associated Molecular Patterns (PAMPs and DAMPs) (9; 10; 11; 12), in addition to several cytokines and inflammation mediators as potent inducers of CCR7 expression in DCs (13; 14; 15). Surprisingly,

although DCs have been discovered more than 20 years ago, the endogenous signals that induce CCR7 expression and trigger their homeostatic migration to lymph nodes remain unknown.

So far, these investigations have exclusively focused on chemical signals. Nevertheless, immune cells such as patrolling DCs that display elevated spontaneous motility even in their non-activated state (16; 17), are also exposed to physical signals. These signals can be mediated by local interactions of immune cells with their environment through specific adhesion (18), or result from global deformations of their cell body and internal organelles (19). We and others have shown that DCs experience and adapt to large shape changes when spontaneously migrating through peripheral tissues or dense tumors (20; 21; 22; 23; 24). Such changes can lead to nuclear deformation events that activate the lipid metabolism enzyme cytosolic phospholipase 2 ($cPLA_2$), a sensor of nuclear envelope stretching (25; 26). This enzyme uses lipids from the nuclear membrane to produce arachidonic acid (AA) that can be converted into Lysophosphatidic acid (LPA), Prostaglandins (PGs) and Leukotriens (LTs) (27; 28; 29; 30), which are known to influence tissue inflammation and thus local immune responses. Activation of $cPLA_2$ further increases actomyosin contractility of cells undergoing deformation, allowing them to effectively migrate into dense tissues (25; 31). Whether the shape changes leading to activation of the $cPLA_2$ pathway have any additional impact on behavior and immune function of DCs has not been addressed.

In this study, we show that the expression of CCR7 in DCs is triggered upon levels of cellular deformation that fall within the range of cell shape changes experienced by tissue-patrolling DCs (21; 23). Such shape changes activate an ARP2/3- and $cPLA_2$-dependent shape sensor that endows DCs with specific immunoregulatory properties, which are distinct from the ones triggered by PAMPS and lead to T cell hypo-responsiveness. We propose that self-imposed shape changes experienced by tissue patrolling DCs act as an endogenous signal to trigger their homeostatic migration to lymph nodes.

Results

CCR7 expression in Dendritic Cells is cell shape-sensitive

We and others have previously observed that DCs migrating within ear explants undergo pronounced cell shape changes resulting from the physical constrains imposed by the environment (23; 32; 21). Quantification of these shape changes revealed that the cell body and nucleus of deformed DCs could reach minimal diameters of about 2 to 4 μm (23). Consistent with these findings, we found that DCs patrolling the mouse ear skin experienced similar shape changes when analyzed by intravital imaging (fig. 1a and supplementary movie 1). We hypothesized that these cell shape changes might impact on the capacity of DCs to express CCR7, and thus to migrate to lymph nodes. To test this hypothesis, we applied precise degrees of cell deformation to DCs using the confiner device illustrated in figure 1b (33; 34). As an experimental model, we chose unstimulated bone-marrow-derived DCs, which express low levels of CCR7 in culture (35; 36), similarly to DCs residing in peripheral tissues (11). Of note, this

is in contrast to purified tissue-resident DCs that rapidly increase CCR7 expression and thus cannot be used for our purpose.

We took advantage of a mouse model harboring a CCR7/GFP reporter gene (37) to evaluate by live imaging the expression dynamics of this chemokine receptor. CCR7/GFP unstimulated DCs were confined at the heights of 3 and 4 μm, which fall in the range of deformation measured for DCs that patrol the mouse skin (fig. 1a and (23; 38)). Fluorescence quantification (supplementary fig. S1a) showed that while GFP expression increased in immature DCs confined at 3 μm height for 4-6 hours, it was not significantly modified in cells confined at 4 μm-height (fig. 1c, d and supplementary movie 2). This was also observed when analyzing the endogenous protein and gene levels of *Ccr7* expression by immunofluorescence and real time quantitative RT-PCR analyses: only immature DCs confined at 3 μm exhibited a significant increase in CCR7 expression (fig. 1e, f). The specificity of the anti-CCR7 antibody was verified using *Ccr7* $^{GFP/GFP}$ DCs (supplementary fig. S2b). A similar observation was made when cells were confined for 30 minutes, harvested and *Ccr7* analyzed 4 hours later by RT-PCR (fig. 1g). These results suggest that imposing a 30 minute-deformation at 3μm-height on unstimulated DCs is sufficient to upregulate CCR7 expression.

Importantly, CCR7 expressed at the surface of DCs confined at 3 μm height was fully functional: addition of its ligand CCL19 at one side of the confinement device triggered chemotaxis (fig. 1h). A significantly smaller response was observed when DCs were confined at 4 μm-height, consistent with the lack of CCR7 expression at this height. Accordingly, DCs confined at 3 μm-height exhibited faster migration speed than the cells confined at 4 μm height close to the source of CCL19 chemokine gradient (fig. 1i). We conclude that deformation of non-activated DCs at 3μm-height leads to up-regulation of CCR7 expression, endowing DCs with the ability to perform chemotaxis along CCL19 gradients.

Shape-sensitive upregulation of CCR7 expression requires the lipid metabolism enzyme cPLA$_2$

We next asked whether CCR7 up-regulation in DCs confined at 3 μm-height required cPLA$_2$, which is activated upon nuclear envelope stretching in a variety of cells (26; 25; 31). Accordingly, we observed that DCs confined at 3 μm-height displayed significant increase in nucleus projected area as compared to non-confined and 4 μm-height confined cells (fig. 2a). To assess the involvement of cPLA$_2$ in the response of DCs to deformation, we either treated them with the AACOF3 cPLA$_2$ inhibitor or knocked down the enzyme using siRNA (supplementary fig. S2a). We found that both cPLA$_2$ inhibition and knock down abrogated the upregulation of CCR7/GFP expression induced by cell confinement (fig. 2b, c). In sharp contrast, cPLA$_2$ inhibition or knock down did not prevent the upregulation of CCR7 expression in response to treatment with the microbial compound lipopolysaccharides LPS (supplementary fig. S2b,

c). These results indicate that this lipid metabolism enzyme is specifically required for CCR7 expression induced by cell deformation, rather than being generally involved in the transcriptional regulation of the *Ccr7* gene. Hence, shape-sensitive induction of CCR7 expression in DCs requires $cPLA_2$.

In zebrafish neutrophils and mammalian epithelial cell lines, $cPLA_2$ activation in response to deformation is thought to result from an increase in nuclear envelope tension (26; 39; 40). Consistent with these findings, we observed that nuclear envelope fluctuations diminished when confining DCs at 3 µm height (supplementary fig. S2d), suggesting a tension increase (41; 42). On the same line, DCs knock out for Lamin (*Lmn*) A/C, a nucleoskeleton protein needed for cells to build up nuclear envelope tension upon confinement (43; 44), did not upregulate CCR7 when confined at 3 µm-height (fig. 2d). In addition, we found that confinement at 2 µm-height, which triggers nuclear envelope ruptures (fig. 2e and supplementary movie 3) and loss of Lamin A/C (fig. 2f) and should thus not lead to a sustained high envelope tension, did not induce *Ccr7* upregulation in DCs (fig. 2g). This was not due to increased cell death, which exhibited low rates at the three confinement heights (< 8% of death in all confinement conditions). DCs confined at 2 µm-height did not display any sign of damage since they were able to upregulate *Ccr7* expression upon LPS treatment (supplementary fig. S2e). These results argue in favor of CCR7 expression being upregulated downstream of $cPLA_2$ activation upon an increase in nuclear envelope tension. Consistently, quantification of $cPLA_2$ subcellular localization revealed that the enzyme was accumulated in the nucleus of DCs confined at 3 µm-height, and not at 4 or 2 µm (fig. 2h), and $cPLA_2$ nuclear translocation was not observed in *Lmn A/C* ^{KO} DCs confined at 3 µm-height (fig. 2i). We conclude that DCs upregulate CCR7 expression when experiencing cell shape changes that enhance the tension of their nuclear envelop and thereby activate $cPLA_2$.

Induction of CCR7 expression in response to shape changes is tuned by the ARP2/3 complex

Lmn A/C is part of the LINC complex that connects the nucleoskeleton to the actin cortical cytoskeleton (45; 46; 47). Such connection is needed for the actin cytoskeleton to exert mechanical forces on the nucleus and might contribute to increase nuclear envelope tension. We therefore investigated whether ARP2/3 was needed for induction of CCR7 expression upon DC change of shape. Treatment of DCs with the ARP2/3 inhibitor CK666 impaired the upregulation of *Ccr7* expression (fig. 3a) and the nuclear accumulation of $cPLA_2$ (fig. 3b) upon confinement at 3 µm-height. Similar results were obtained when using DCs knock out for WASP, which was recently shown to activate ARP2/3 in the DC perinuclear area (48). We found that WASP^{KO} DCs did not upregulate CCR7 surface expression upon confinement at 3 µm-height (fig. 3c), a phenotype that resembled the one of CK666-treated DCs. These results suggest that DCs respond to cell shape changes by activating ARP2/3 for nucleation of perinuclear branched actin, which will ultimately lead to activation of $cPLA_2$ and upregulation of CCR7 expression.

To strengthen these results, we assessed the response of DCs knock out for the ARP2/3 inhibitor Arpin (*Arpin* $^{flox/flox}$ x CD11c-CRE) (49). Remarkably, we found that Arpin^{KO} immature DCs underwent a shift in their sensitivity to cell deformation as they upregulated *Ccr7* when confined at 4 instead of 3 µm-height (fig. 3d). Arpin^{KO} immature DCs confined at 4 µm-height accumulated cPLA$_2$ in their nucleus almost to the same extent observed in DCs from Arpin^{WT} confined at 3 µm-height, suggesting that this enzyme is activated in Arpin^{KO} cells already at the height of 4 µm (fig. 3e). Of note, induction of *Ccr7* expression in Arpin^{KO} DCs was cPLA$_2$-dependent, as observed in wild-type cells (fig. 3f). Live-imaging revealed that, when confined at 4 µm-height, Arpin^{KO} DCs exhibited a cloud of perinuclear F-actin that was not observed in their wild-type counterpart under the same height but observed in wild-type cells confined at 3 µm (fig. 3g, supplementary movie 4, and supplementary fig. S2f for quantification approach). These data show that the activity of ARP2/3 determines the sensitivity of DCs to confinement, defining a threshold for cPLA$_2$ activation and induction of CCR7 expression in response to cell shape changes.

Increased homeostatic migration of Dendritic Cells with elevated ARP2/3 activity

CCR7 up-regulation in DCs triggers their migration to lymph nodes. By restraining cPLA$_2$ activation and downstream induction of CCR7 expression in response to shape sensing. Arpin might therefore act as a negative regulator of homeostatic DC migration to lymph nodes. This process could limit the number of DCs that become CCR7-positive, and thus migrate to lymph nodes, upon the shape changes they experience while patrolling peripheral tissues (46; 21). To test this hypothesis, we assessed by flow cytometry whether Arpin deficiency altered the number of migratory DCs present in skin-draining lymph nodes at steady state, i.e. in absence of any external stimulation. This experiment showed that the number of Arpin^{KO} migratory DCs found in lymph nodes was increased, as compared to wild-type migratory DCs (fig. 4a, b). This particularly concerned the main subtype of conventional DCs (cDCs) that migrate to lymph nodes in homeostasis: migratory cDC2s. No such difference was observed when quantifying lymph node-resident DCs. Analysis of DC numbers in the skin showed a slight decrease of Arpin^{KO} cDC2s (fig.4c, d), excluding that increased numbers of migratory cDC2s in lymph nodes result from increased number of cDC2s present in the skin of Arpin^{KO} mice. Taken together, these data are consistent with Arpin^{KO} cDC2s leaving the skin at higher frequency as compared to wild-type cells, leading to increased numbers of cDC2s in lymph nodes at steady-state.

ARP2/3 deficiency was shown to regulate immune cell migration and chemotaxis *ex vivo* and *in vivo* (50; 51; 52; 53). We therefore assessed whether Arpin^{KO} DCs displayed enhanced chemotactic migration along CCL19 gradients in collagen gels, as this could also account for their increased migration to lymph nodes at steady state. Noticeably, no difference was observed in the ability of LPS-treated DCs to express surface CCR7 and follow CCL19 gradients (fig. 4e, f, g), they even displayed

slower migration phenotype as compared to their WT counterparts (fig. 4h). We conclude that the levels of ARP2/3 activity tune the number of DCs that migrate to lymph nodes at steady state by controlling $cPLA_2$ activation and downstream CCR7 expression in response to cell shape sensing. These data suggest a working model where steady state migration of DCs to lymph nodes could result from the nuclear massaging events they experience while migrating through peripheral tissues. Such nuclear massaging would activate ARP2/3 and $cPLA_2$, leading to CCR7 expression and migration to lymphatic vessels.

Induction of CCR7 expression in response to shape sensing involves Ikkβ *and* NFκB

The only pathway that has been described so far as controlling steady state migration of cDC2s from the skin to lymph nodes is the NFκB pathway driven by its activating kinase Ikkβ (*Ikbkb*) (6). This prompted us investigating whether Ikkβ was needed for CCR7 upregulation upon shape sensing in DCs. Remarkably, we found that confinement at 3 µm-height did not lead to *Ccr7* upregulation in DCs treated with the Ikkβ inhibitor BI605906 nor in *Ikbkb* knock out cells (fig. 5a, b). Of note while NFκB nuclear translocation was compromised in confined DCs lacking $cPLA_2$, Ikkβ inhibition did not affect nuclear accumulation of $cPLA_2$ (fig. 5c, d). These findings show that $cPLA_2$ acts upstream of Ikkβ and NFκB nuclear translocation to trigger upregulation of CCR7 expression upon shape sensing in DCs. They highlight the existence of an ARP2/3-$cPLA_2$-NFκB axis controlling steady state migration of DCs to lymph nodes in response to shape sensing.

Cell shape sensing through the ARP2/3-$cPLA_2$-NFκB *axis reprograms gene transcription in DCs*

The involvement of NFκB in shape sensing by DCs suggest that these events of cell deformation might have a global effect on DC transcription beyond the upregulation of *Ccr7* expression. Such effect may define the immunoregulatory properties of DCs migrating to lymph nodes upon activation of the $cPLA_2$ shape sensing pathway thereby impacting on the type of T cell response they induce. To address this question, we analyzed by bulk RNAseq the transcriptome of DCs expressing or not $cPLA_2$ (*Pla2g4a*) and confined at 3 µm-height, non-confined cells were used as negative controls. The overview of the gene expression profiles obtained showed that, while non-confined wild-type and $cPLA_2$ KO cells seemed very similar, confined $cPLA_2$ KO cells had lost a large proportion of the genes induced by confinement in their wild-type counterpart (fig. 6a). Principal component analysis provided a clear quantitative assessment of this effect: while non-confined wild-type and $cPLA_2$ KO samples clustered together with similar PC1 and PC2 values, confined cells showed very different values in WT and $cPLA_2$ KO DCs (fig. 6b). Focusing on the genes that significantly varied (p-value <= 0.05 and fold-change >= 1.5) between confined and non-confined conditions, we observed that ~2000 and ~1800 genes were up and

downregulated in non-activated wild-type DCs confined at 3 µm-height, respectively (fig. 6c, see red and yellow ellipses). Comparison of cPLA$_2$-sufficient (*Pla$_2$g4a* $^{flox/flox}$ CD11c-CRE-/-) and deficient (*Pla$_2$g4a* $^{flox/flox}$ CD11c-CRE+/-) DCs showed that a large fraction (about half) of the genes that were up- or downregulated by confinement in wild-type cells were not significantly changed in cPLA$_2$ KO DCs (fig. 6c, see blue and green ellipses). Pathway analysis revealed that the genes whose upregulation was lost in cPLA$_2$ KO DCs were enriched for distinct innate immunity-related (cytokines, interferon, interleukins, and NFκB activation) as well as antigen processing pathways (fig. 6d). Altogether, these results suggest that cell-shape sensing leads to a transcriptional reprogramming of DCs and affects expression of genes related to their immunomodulatory properties in a manner that mostly depends on cPLA$_2$.

In agreement with our findings above, we observed that *Ccr7* upregulation was fully lost in cells lacking cPLA$_2$, which even rather showed a decrease in *Ccr7* levels upon confinement (fig. 6e – note that since *Ccr7* was almost not expressed in non-confined DCs, this further reduction might not have a strong functional meaning). Strikingly, among the genes following the same expression pattern (not expressed in non-confined DCs and induced by confinement in wild-type but not in cPLA$_2$ KO DCs) were two genes associated with ARP2/3-dependent actin nucleation (*Actr2*, *Actr3*) as well as the Ikkβ gene (*Ikbkb*) (fig. 6f). Of note, several genes associated to the type I interferon (IFN) response, including several IFN related genes and IFN-sensitive genes (ISGs), also followed the same expression pattern than *Ccr7* and *Ikbkb* *(*fig. 6g). This result is in agreement with previous findings highlighting that cDC2s migrating from the skin to lymph nodes at steady state exhibited a type I IFN signature (54), in addition to their NFκB one (6). Our findings are consistent with a model where the ARP2/3-cPLA$_2$-NFκB cell-shape sensing axis leads to transcriptional changes that (1) upregulates *Ccr7* expression, promoting the homeostatic migration of DCs to lymph nodes and (2) endows these cells with the capacity to harbor a specific immunoregulatory phenotype.

Cell shape-sensing endows DCs with immunoregulatory properties distinct from those induced by microbes

Beyond type I IFN, we found that distinct genes linked to innate sensing pathways were upregulated in a cPLA$_2$-dependent manner in DCs confined at 3 µm-height (fig. 6h). To assess whether this was specific of DCs experiencing shape changes or more generally applied to activated DCs, we evaluated the cPLA$_2$ dependency of the transcriptome of LPS-treated cells. Astonishingly, this experiment showed that cPLA$_2$ had no significant impact on the global gene expression pattern induced upon DC treatment with LPS (fig. 7a and b, see also PCA in fig. 6b and Volcano plots in fig. S3a). In agreement with this result, when comparing the expression of the cPLA$_2$ gene itself (*Pla$_2$g4a*) and genes related to the cPLA$_2$

pathway, we observed that several of them were more up-regulated in DCs confined at 3 µm-height as compared to LPS-treated cells (fig. 7c). Among the genes that significantly varied (p-value <= 0.05 and fold-change >= 1.5) between wild-type samples, about 1500 genes were upregulated in both LPS and confined cells (fig. 7b). Importantly, induction of these genes was lost in confined but not in LPS-treated $cPLA_2$ KO DCs, showing that the same large set of genes is controlled by different pathways in response to these two stimuli.

Pathway analysis highlighted that the genes specifically upregulated in response to LPS, but not to confinement, were mainly associated with the immune response (1221 genes, fig. 7b blue ellipse and fig. 7d). The genes specifically upregulated in response to confinement belonged to lipids metabolism and antigen presentation (489 genes, fig. 7b red ellipse and fig. 7e). Of note, although both confinement and LPS responses led to up-regulation of the NFκB pathway (fig. 7d, e pathways in orange), the precise genes concerned were distinct (fig. 7f). In particular, we observed that the expression of proteasome (PSM) genes belonging to the NFκB pathway was induced by LPS treatment but not by confinement. Altogether these results highlight that shape sensing in DCs transcriptionally reprograms these immune cells in a way distinct from microbial activation and with a different requirement for $cPLA_2$.

Noticeably, we observed that LPS-activated DCs expressed higher levels of genes encoding for cytokine and co-stimulatory molecules (examples in supplementary fig. S3b). We experimentally confirmed that IL1b, IL12a, IL27, and IL15 were indeed secreted at higher levels in LPS-activated DCs as compared to confined cells (supplementary fig. S4c bottom). In addition, cytometry analysis of CD80, CD86, and MHCII surface expression showed that these co-stimulatory molecules were induced at lower levels in confined DCs, as compared to LPS-activated cells (fig. 7g). These results suggest that confined DCs might be less potent than LPS-treated cells for T lymphocyte activation. To address this question, we loaded the two types of DCs with the ovalbumin (OVA) peptide and incubated them with OT-II transgenic T cells, which specifically recognize these MHC II-peptide complexes. These experiments unambiguously showed that confined DCs were less efficient than LPS-treated cells in T lymphocyte activation, although cell viability was comparable in both conditions (fig. 7h, supplementary fig. S3d). A similar result was obtained performing Mixed Leukocyte Reactions (MLR) (supplementary fig. S3e). These findings confirm that DCs that experience shape changes are in a distinct activation stage as compared to microbe-activated ones, displaying a milder T cell activation capacity. They are consistent with the tolerogenic properties that had been previously proposed for DCs migrating to lymph nodes in homeostasis (55).

Discussion

Here we show that expression of the chemokine receptor CCR7, responsible for the directed migration of immune cells to lymph nodes, can be triggered in DCs by changes in their shape. Shape sensing is under the control of the lipid metabolism enzyme $cPLA_2$, whose activation is induced at a range of cell deformation similar to the one observed in DCs patrolling peripheral tissues such as the skin (38; 23) or the tumor microenvironment (56). Activation of $cPLA_2$ requires nuclear envelope tensing, which depends on branched actin nucleation by ARP2/3. $cPLA_2$ in turn activates IKKβ-dependent nuclear translocation of NFκB, leading to the expression of a set of immunomodulatory genes among which is *Ccr7*. We propose that this ARP2/3-$cPLA_2$-NFκB axis spontaneously activates as a result of the successive changes in shape that DCs experience while patrolling tissues at steady-state, thereby triggering their homeostatic migration to lymph nodes. These findings might explain why, despite two decades of research, the signals that lead to DC migration to lymph nodes at steady-state had remained unknown: rather than sensing (bio)chemical signals, patrolling DCs might sense the shape changes imposed by the physical constrains of their environment.

We found that the ARP2/3-$cPLA_2$-NFκB shape sensing axis modulates both the chemotactic and immunomodulatory properties of DCs. This result suggests that the cell shape changes that DCs experience while migrating in peripheral tissues might influence their ability to shape T lymphocyte responses once in lymph nodes. Indeed, we observed that confined DCs express less pro-inflammatory cytokines as compared to the ones that are typically expressed upon treatment with PAMPs. Furthermore, although confined DCs express co-stimulatory molecules such as CD80 and CD86, their surface levels are decreased as compared to the ones observed in LPS-treated cells. This is consistent with confined DCs being less efficient in triggering T cell activation and proliferation, and compatible with the tolerogenic function that has been proposed for DCs at steady state. It is also in accordance with our data showing the requirement of $cPLA_2$ to trigger Ikkβ and NFκB activation, which are known to control homeostatic DC migration to lymph nodes and thereby prevent autoimmune responses (6). Noticeably, our results highlight that the ARP2/3-$cPLA_2$-NFκB shape sensing pathway is not involved in transcriptional reprogramming of DCs by LPS, even though confined and LPS-treated DCs share part of their transcriptional program.

We postulate that self-activation of the ARP2/3-$cPLA_2$-NFκB axis originates from the successive events of deformation DCs undergo as they move through the complex environment of peripheral tissues. Indeed, these deformation events would induce a 'nuclear massage' and thereby activate the shape-sensing pathway with a specific temporal pattern. Although we have not yet characterized the precise

temporal pattern that leads to activation of the ARP2/3-cPLA$_2$-NFκB axis *in vivo*, we propose that this shape sensing pathway might act as an internal clock. Such clock would help DCs "measuring the time" they have spent patrolling tissues as a function of the number and/or extent of deformation events they have experienced. This implies that DCs that patrol dense tissues, i.e. which impose more pronounced shape changes on their cell body, might exhibit reduced time of residency and/or altered immunoregulatory properties. This might be the case, for example, in tissues such as in the skin, the lungs, fibrotic tissues or tumors. Interestingly, a recent study has identified a mouse tumor-resident DC population, referred to as "mature reg (mReg) DCs", which shares similarities with our confined DCs: both populations harbor a mature phenotype, characterized by the presence of CCR7 on their surface, but also express numerous immunoregulatory genes (57). Future studies aimed at analyzing the role of cPLA$_2$ in the emergency of mReg DCs should help evaluating the contribution of the shape-sensor pathway to anti-tumor immunity.

In conclusion, we propose that the self-imposed nuclear 'massaging' that DCs experience while patrolling their environment at steady state might promote the emergence of a population of migratory DCs that arrive to lymph nodes harboring specific immunomodulatory properties, compatible with their tolerogenic function. We foresee that this ARP2/3-cPLA$_2$-NFκB shape-sensing axis might also impact the physiology of other cPLA$_2$-expressing cells, for example monocytes, which rely on CCR7 and on the PGE-producing enzyme COX to home to tissues at steady-state (58), or tumor cells, which use CCR7 to invade healthy tissues by first migrating to lymph nodes (59; 60).

Acknowledgments:

Funding: This project has received funding from the European Union's Horizon 2020 research and innovation program under the Marie Skłodowska-Curie grant agreement No 666003. This work has also received support under the program «Investissements d'Avenir» launched by the French Government, from la Fondation de la Recherche Médicale (Team Grant SMC202006012351 to AMLD). ANR-10-IDEX-0001-02 PSL. P.J.S received the support of Human Frontier Science Program (HFSP) RGP0032-2022 and Forschungszentrum Medizintechnik Hamburg (FMTHH, grant 04fmthh2021). H.D.M received the support of ANR-20-CE15-0023 (InfEx). High-throughput sequencing was performed by the ICGex NGS platform of the Institut Curie supported by the grants ANR-10-EQPX-03 (Equipex) and ANR-10-INBS-09-08 (France Génomique Consortium) from the Agence Nationale de la Recherche ("Investissements d'Avenir" program), by the ITMO-Cancer Aviesan (Plan Cancer III) and by the SiRIC-Curie program (SiRIC Grant INCa-DGOS-465 and INCa-DGOS-Inserm_12554). Data management, quality control and primary analysis were performed by the Bioinformatics platform of the Institut Curie. The RNAseq data analysis was performed by GenoSplice technology (Paris, France). We would like to thank the lab of Dr. Federica Benvenuti and the lab of Pr. Michael Sixt for providing bone marrow from WASP KO mice.

Material and methods:

Mice:

B6: C57BL6/J, provider Charles River, catalogue: #000664.

CCR7-GFP knock in/ knock out mice: from Jackson laboratory, stock number: 027913, bred in our animal facility, original paper: Nakano H et al., 2013. CD11c-Cre mice: bred in our animal facility, original paper: Caton et al., 2007. Arpin knockout mice: were generated by CIPHE in Marsaille, IkkB knockout mice: from our collaboration with Prof.Toby Lawrence, original paper BaratinM et al., 2015. Lmna flox Vav1-Cre mice: From Manel's lab: original mice from José María González Granado, bred in our animal facility, original paper Kim Y, Zheng Y., 2013. $cPLA_2$ KO mice were generated by CIML in Marsaille. Littermates or age-mated mice were used as bone marrow donors; the breeder mice were previously backcrossed to C57BL6 for 7 generations. CD11c-Cre+ mT/mG+ mice used for intravital imaging were from D. Vignjevic (Institut Curie) (original paper: Muzumdar et al. (2007)).

Cells:

Dendritic cells were obtained following a protocol first described by (K. Inaba 1992). Both whole legs from 6 to 8 weeks old mice were flushed to obtain bone marrow. Cells are maintained in culture during 10 days in IMDM medium (Sigma-Aldrich, Darmstadt, Germany) containing 10% FBS decomplemented and filtered (Biowest, Nuaillé, France), 20 mM L-glutamine (Gibco, Waltham, Massachusetts, USA), 100 U/ml penicillin–streptomycin (Gibco, Waltham, Massachusetts, USA), 50 µM 2-mercaptoethanol (Gibco, Waltham, Massachusetts, USA), and 50 ng/ml of GM-CSF containing supernatant obtained from transfected J558 cells tested by ELISA, as previously described by (Faure-Andre 2008). At days 4 and 7 of culture, cells are detached using PBS-EDTA (5 mM) and replated at $0.5{:}10^6$ cells per milliliter of medium. At day 10, 90% of adherent cells express CD11c, an integrin family member, as well as MHC class II at medium levels which is specific to dendritic cells (35). The obtained cells can be used at day 10 or 11 as immature cells. The generation of dendritic cells from bone marrow supplemented with GM-CSF is a well-defined protocol but it promotes the differentiation of three cell types: granulocytes, macrophages, and dendritic cells (61) but they can separated during the cell culture based in their adhesion. Granulocytes are eliminated during the culture since they are non-adherent, whereas, macrophages are much more adherent than the other two cell types and stick to the bottom of the plate and thus we recover the semi-adherent dendritic cells at the last day of culture.

Dendritic cells maturation:

When using mature cells (mainly as a positive control for maturation profile of dendritic cells): Day 10 cells (which are immature when we recover them), are stimulated with 100 ng/ml of

lipopolysaccharide (LPS) (Salmonella enterica serotype typhimurium; Sigma, Darmstadt, Germany) for 25 minutes and washed three times with complete medium, re-plated in fresh medium, left overnight in the incubator and then used. LPS-activated dendritic cells have higher levels of expression of the costimulatory molecules CD86 and CD40 as well as the chemokine receptor CCR7.

6-well plate confiner:

Dendritic cell confinement was performed using a 6-well plate confiner described by (Y.-J. Liu 2015) that allows the recovery of large number of cells and the simultaneous imaging of several conditions. To make the polydimethylsiloxane (PDMS, RTV615) pillars at a certain height, 12 mm glass coverslips were sonicated in methanol, washed in ethanol then plasma treated and placed on the top of a PDMS mixture on top of wafer molds that contain the pillars at the desired height. The PDMS mixture is composed of PDMS A/crosslinker B at 1/10 W/W. The height of the PDMS pillars is what determines the height of confinement of the cells between the coverslip and the bottom substrate. After adding the coverslips to the wafers, they are baked at 95° for 15 minutes, then carefully removed using isopropanol. Then they are washed again with isopropanol, dried well and plasma treated for 2 minutes. They are then incubated with non-adhesive pLL-PEG (SuSoS, PLL (20)-g [3.5]-PEG (2)) at 0.5mg/ml in 10mM HEPES pH 7.4 buffer for one hour at room temperature. The coverslips are then washed well with water to remove all the remaining PEG and incubated in cell's medium for at least 2 hours before the confinement starts. To make the confinement steps, we use a modified version of a classical 6-well plate cover; large PDMS pillars were stuck on the coverlid (these are the ones which will hold the fabricated coverslips). These large pillars will push the coverslips from the top of the lid to confine the cells. 6-well plates with glass bottom can be used in case of imaging of the cells (MatTek corporation, P06G-1.5-20-F).

Collagen gels:

Collagen gels experiments were performed based on what was described previously (62) . DCs were mixed at 4 °C with 1.6% bovine collagen type I (Advanced BioMatrix). 40 µls of the mix were deposited on a 35 mm glass-bottom dish and the drop was homogenized while covered with a 12 mm glass slide. The sample was incubated at 37 °C for 20 min to allow collagen polymerization. To generate the CCL21 gradient, 2 ml of DC medium containing 200 ng ml^{-1} of CCL21 was added to the plate. Cells were imaged overnight with a phase contrast with 10 objective and a frequency of 1 image per 2 min. Contiguous positions were stitched using the FIJI plugin Grid/collection stitching (63) to extract individual cell tracks. The mean image of the movie was subtracted from every time point and white objects in a dark background were detected. Resulting movies were processed using the FIJI plugin Filter Mean (Intensity 3) and cells were tracked using custom software (64).

Live cell imaging:

Live Time-lapse recordings were acquired with 20x (NA 0.75) dry objective, Nikon video-microscopy, for 4-6 hours at 37 °C with 5% CO2 atmosphere. Or by confocal microscope (Leica DMi8, SP8 scanning head unit) with 40x (NA 1.3) oil objective with a resolution of 1024x1024 pixels. Both microscopes were controlled by Meta Morphe software. Image analysis was performed using Imag eJ software (65) (NIH, http://rsb.info.nih.gov/ij/index.html).

For GFP quantification, imaging was done using both transmission phase and GFP. Images corresponding to each time point of interest were collected in each condition, the outline of each cell was drawn by hand on the trans images, then the mean GFP signal was calculated on the corresponding GFP image using a homemade macro; mean intensity of each cell was subtracted from the average intensity of the background, then multiplied by cell's area to calculate total GFP intensity per cell. Of note, only cells with intensity higher than the background were plotted (percentage of cells is indicated in the legends).

Constructs:

NLS_GFP: pTRIP-SFFV-EGFP-NLS (NLS-GFP hereafter) was generated introducing the SV40 NLS sequence (PKKKRKVEDP) by overlapping PCR at the C-terminal of GFP in pTRIP-SFFV that were from the lab of N.Manel (23) .

Lap2b: the plasmid was obtained by cloning LAP2b from pN2-EGFP-LAP2b (available on Addgene) into pTRIP-SFFV-EGFP that were from the lab of N.Manel using 2 restriction enzymes BsrGI and KpnI.

Lentivirus transduction:

Transduced dendritic cells were obtained by transfection of BMDCs from C57BL/6 mice were 1million cells/2ml medium were plated. At day 4, 40ml of fresh pTRIP-SFFV-GFP-NLS lentivector supernatant were loaded in Ultra-Clear Centrifuge tubes (Beckman Coulter) and ultracentrifuged at 100,000g in a SW32 rotor (Beckman coulter) for 90 minutes at 4°C and re-suspended in 400µl of in DC medium. 200µl of ultracentrifuged virus were used to infect one well of cells in presence of 8µg/ml of Protamine. Cells were then left for 48h, then washed to remove the viral particles and left in new medium till day 10 of culture.

NE fluctuation measurements:

Nuclei of live cells expressing EGFP-LAP2b (transduced with pTRIP-SFFV-EGFP-LAP2b) were recorded on a Leica DMI8 microscope, equipped with CSU-X1 Yokogawa spinning disk module. The acquisition was realized with a 63x oil objective (N.A. 1.40) and collected by the Hamamatsu Orca flash 4.0 camera.

Movies at high temporal resolution were then acquired with a 488 nm laser at 3% (exposure time 200 milliseconds) at the rate of 1 frame every 250 milliseconds for 700 timeframes using a high frame rate acquisition mode. The position of each nucleus was corrected for linear and rotational drift using the Stackreg plugin of the ImageJ/Fiji software. NE fluctuations were calculated by measuring the square root of the mean square displacement (MSD), expressed in µm. To precisely position the NE, line scans across the NE (intensities along a line of 1 pixel in width perpendicular to the NE) were made at 4 different positions per nucleus along the NE. For each point along the NE and for each time point in the movie, the point of maximum intensity was calculated on the line scan and a parabola was fitted on 5 points before and after the maxima to determine the localization of the NE with a sub-pixel resolution. For a first round of analysis, the mean position was taken as the average across all time points. Points with a displacement larger than twice the average displacement were considered outliers and removed from analysis. A new mean position was calculated from non-outliers' points and used as reference to calculate the displacement at each time point. The square root of the MSD was calculated as follows: The square root of the MSD was taken as one measure for the fluctuation of the NE. Each point along the NE contributes one measure. The values per cell were obtained by averaging the values of the corresponding kymographs. A floppy and thus less tensed, membrane is expected to fluctuate more, whereas a membrane under tension exhibits no or diminished fluctuations. Important to mention that in our hands, transduced –iDCs seemed to have bigger area than non-transduced cells.

Drugs and Reagents:

For live imaging experiments: NucBlue (Hoechst33342) from Thermo fischer (R37605) to mark the DNA. For drug treatments: AACOCF3 (selective phospholipase A_2 inhibitor, Tocris #1462-5), CK666 (selective Arp2/3 inhibitor, Tocris #3950), BI605906 (selective IKKβ inhibitor #53001).

Immunofluorescence microscopy:

The staining was done directly on the confinement plate to not affect the expression of the markers of interest. After removing the confinement led, samples were fixed directly with 4% paraformaldehyde for half an hour, permeabilized with 0.2% Triton X-100, and then incubated overnight with the primary antibodies at 4°. The next day, samples were washed with PBS and incubated with the corresponding secondary antibodies for one hour, then washed three times with PBS and mounted with fluromount solution. Imaging was done using confocal microscope (Leica DMi8, SP8 scanning head unit) with 40x (NA 1.3) oil objective with a resolution of 1024x1024 pixels. The following primary antibodies were used for the IF staining: anti-CCR7 (abcam #ab32527), anti-laminA/C (Sigma #SAB4200236), anti-cPLA$_2$ (abcam #ab58375), anti-NF-κB P65 (cell signalling #mAB 8242), Alexa Fluor-coupled Phalloidin (Invitrogen).

Calculation of the florescence intensity:

Images were acquired with SP8 confocal microscope, then Z stacks of usually 0.33 µm as a step size were made for each position, with a home-made macro, the plan of the nucleus was used to quantify the florescence intensity by making a mask on both the nucleus (taking the Dapi channel) and the cell (taking the phalloidin channel) and intensity was calculated.

Transfection and SiRNA oligonucleotides:

Bone marrow derived dendritic cells at day 7 ($3x10^6$) were transfected with 100µl of the Amaxa solution (Lonza) containing siRNA (control or target-specific) following the manufacturer's protocol. Cells were further cultured for 48-72 hours. At the day of the experiment wells were detached with medium, some cells were collected to check the efficacy of the Si step by either western blot or RT-qPCR protocols. The following SMARTpool siRNAs were used: SMARTpool: ON-TARGETplus *Pla_2g4a* siRNA (Dharmacon # L-009886-00-0010) and ON-TARGETplus Non-Targeting Control Pool (Dharmacon # D-001810-10-20).

RT-qPCR:

After removing the confinement, the lysis buffer was added directly to recover the confined cells, taking in parallel control cells that were not confined.

RNA extraction was performed using RNeasy Micro RNA kit (Qiagen), according to the manufacturer's protocol. cDNA was produced using the high capacity cDNA synthesis kit (thermo fisher), according to the manufacturer's protocol, starting from 1 µg of RNA. Quantitative PCR experiments were performed using Taqman Gene Expression Assay (Applied Biosystems) and carried out on a Lightcycler 480 (Roche) using the settings recommended by the manufacturer.

The following primers were used: Mm99999130_s1 for CCR7, Mm01284324_m1 for Pla_2g4a and Mm99999915 for GAPDH as a control. The expression of each gene of interest was assessed in immature non-confined cells. Samples were run in triplicate for each condition. Data were subsequently normalized to GAPDH values, and to the values obtained in control immature cells were used as a base unit equal to one, thus allowing for display of the data as "fold-greater" than the immature cells. The fold change was calculated by the formula $2^{-\Delta\Delta CT}$.

Flow cytometry analysis:

To characterize the expression of some surface markers on the dendritic cells after confinement we used the FACS approach. In brief, after confining the cells, the confiner was removed and cells were recovered directly by gently washing with medium. Non-confined cells activated with LPS were also

taken as controls. Cells were re-suspended in the buffer (PBS BSA 1% EDTA 2mM). After blocking with Fc antibody (BD #553142) and live/dead staining kit (Thermo # L34966) for 15 minutes, cells were stained with the desired antibodies for 20 minutes (at 37° for CCR7 staining and at 4° for the rest). Cells were then washed three times and re-suspended in the staining buffer. Flow cytometry was performed on LSRII (BD) and analyzed using FlowJo software version 10. Mean florescent values of each condition were plotted with Graphpad Prism version 8. The following antibodies were used: anti-CD80 (BD # 553769), anti-MHCII (Ozym # BLE107622), anti-CD86 (Ozyme # BLE105037), anti-CD11c (BD # 550261) with the corresponding isotypes to each antibody.

For the T-cell presentation assay: OVA peptide (Cayla #vac-isq) was added to each condition with the corresponding concentration, cells were then confined for four hours, then recovered by washing with medium and counted, T-cells which were purified from OTII mice were added to the recovered dendritic cells with a ratio of 10 to 1 respectively. Then next day, half of the medium was recovered and staining for T-cells was don. Cells were stained in 2mM EDTA, 5%FBS in PBS following the same protocol as before. Then 2 days later, the rest of the medium was recovered and sating for the T-cells was done.

Flow cytometry was performed on LSRII (BD) and analyzed using FlowJo software version 10. Percentage values were plotted with Graphpad Prism version 8. The following antibodies were used: anti-CD4 (BD # 553051), anti-CD69 (eBioscience # 48-0691-82), anti-TCR (BD # 553190).

MLR protocol:

For the mixed lymphocyte reaction (MLR) assay, allogeneic CD3+ T cells were isolated using a pan T-cell isolation kit (Miltenyi) and cultured in 96-well plates with DCs at different ratios. DCs were confined at the height of 3 µm for 4 hours then recovered and counted before adding the T-cells. Cells were cultured for 3 days, and proliferation was assessed by the addition of CFSE.

On the day of the analysis (3 days after the coculture), cells were stained in 2mM EDTA, 5%FBS in PBS following the same protocol as before and sating for the T-cells was done. Flow cytometry was performed on LSRII (BD) and analyzed using FlowJo software version 10. Percentage values were plotted with Graphpad Prism version 8.

RNA seq:

After removing the confinement, the lysis buffer was added directly to recover the confined cells, taking in parallel control cells that were not confined.

RNA extraction was performed using RNeasy Micro RNA kit (Qiagen), according to the manufacturer's protocol. The samples were checked for the quality of the extracted RNA before sending them to the NGS-sequencing platform in the institute Curie RNA sequencing libraries were prepared from 300ng to 1µg of total RNA using the Illumina TruSeq Stranded mRNA Library preparation kit and the Illumina Stranded mRNA Prep Ligation kit which allow to perform a strand specific RNA sequencing. A first step of polyA selection using magnetic beads is done to focus sequencing on polyadenylated transcripts. After fragmentation, cDNA synthesis was performed and resulting fragments were used for dA-tailing and then ligated to the TruSeq indexed adapters (for the TruSeq kit) or RNA Index Anchors (for the mRNA Ligation kit). PCR amplification was finally achieved to create the final indexed cDNA libraries (with 13 cycles).

Individual library quantification and quality assessment was performed using Qubit fluorometric assay (Invitrogen) with dsDNA HS (High Sensitivity) Assay Kit and LabChip GX Touch using a High Sensitivity DNA chip (Perkin Elmer). Libraries were then equimolarly pooled and quantified by qPCR using the KAPA library quantification kit (Roche). Sequencing was carried out on the NovaSeq 6000 instrument from Illumina using paired-end 2 x 100 bp, to obtain around 30 million clusters (60 million raw paired-end reads) per sample.

RNA seq data analysis:

The RNAseq data analysis was performed by GenoSplice technology (Paris, France). Raw data are available at GEO under the number: GSE207653.

Analysis of sequencing data quality, reads repartition (e.g., for potential ribosomal contamination), inner distance size estimation, gene body coverage, strand-specificity of library were performed using FastQC, Picard-Tools, Samtools, and RSeQC. Reads were mapped using STAR [PMID: 23104886] on the mm39 genome assembly.

Gene expression was estimated as described previously [PMID: 34495298] using Mouse FAST DB v2021_2 annotations. Only genes expressed in at least one of the two compared conditions were analyzed further. Genes were considered as expressed if their Fragments Per Kilobase Million (fpkm) value was greater than fpkm of 98% of the intergenic regions (background). Analysis at the gene level was performed using Deseq2[PMID: 25516281]. Genes were considered differentially expressed for fold-changes ≥1.5 and p-values ≤0.05. Pathway analyses and transcription factor network analysis were performed using WebGestalt 0.4.4 (66)[PMID: 31114916] merging results from upregulated and downregulated genes only, as well as all regulated genes. Pathways and networks were considered significant with p-values ≤0.05.

The graphics (heat map, pca, scatter and volcano plots) were generated using R v4.2.1 with the help of ggplot2 and ComplexHeatmaps [PMID:27207943] packages. The heat maps were created using the Z-score of Deseq2 normalized counts. The scatter plots represent the log2 fold-change of a comparison against another.

In vivo analysis of dendritic cell's subtypes:

Littermates at the age of 12-16 weeks of Arpin wild type (flox/flox cre-/-) and knockout (flox/flox cre+/-) mice were used. Both males and females.

To collect cells from the skin: 1 cm^2 part of the skin was cut with the help of a stencil, and transferred to an Eppendorf tube. 1ml of 0.25 mg/ml of liberase (Sigma #5401020001) and 0.5 mg/ml of DNAse (Sigma #10104159001) in 1 ml RPMI medium (sigma). The skin was cut using scissors and incubated 1-2 hours at 37°.

To collect cells from the lymph nodes: axial and branchial lymph nodes were removed. Then they were transferred to an Eppendorf tube containing 500µl of RPMI medium, DNAse was added at concentration of 0.5 mg/ml and collagenase at 1 mg/ml. The nodes were further cut with scissors and incubated 20 minutes at 37°.After, cells were re-suspended in PBS 0.5% BSA 2mM EDTA at 4°. Cells were filtered with cells strainer of 100 µm in a tube of 50ml. cells were centrifuged and then stained following the same protocol as explained before.

The following antibodies were used:

Anti-CCR7 (Biolegend #120114), anti-cd11c (eBioscience #25-0114-81), anti-cd326 (Biolegend #118217), anti-cd86 (BD pharmingen #553692), anti-cd11b (Biolegend #101237), anti-MHCII (eBioscience #56-5321-80), anti-cd45 (eBioscience #61-0451-82), ant-cd8a (BD bioscience #553035), anti-cd103 (eBioscience #46-1031-80). Flow cytometry was performed on LSRII (BD) and analyzed using FlowJo software version 10. Percentage values were plotted with Graphpad Prism version 8.

Intravital imaging of dendritic cell's migration in ear skin dermis by 2P

Data previously generated (Moreau et al, Dev Cell 2019) were reanalyzed to estimate the deformation experienced by DCs migrating in the skin. Two-photon intravital imaging of the ear dermis was performed as previously described (Filipe-Santos et al., 2009), on bone-marrow chimeras reconstituted with 50% of CD74WT bone marrow (from mTmGflox/flox CD11c-Cre+ animals: DCs are GFP+) and 50% $CD74^{KO}$ bone marrow (from CD11c-EYFP animals: DCs are YFP+). Imaging was done at least 8 weeks after irradiation (9Gy) and bone-marrow reconstitution to ensure steady state. In brief, mice were anesthetized and placed on a custom-designed heated stage and a coverslip sealed to a

surrounding parafilm blanket was placed on the ear, to immerge a heated 25X/1.05 NA dipping objective (Olympus). Imaging was performed using an upright FVMPE-RS microscope (Olympus). Multiphoton excitation was provided by an Insight DS + Dual laser (Spectra-Physics) tuned at 950 nm. Emitted fluorescence was split with 520, 562 and 506 nm dichroic mirrors and passed through 593/40 (mTom) and 542/27 (YFP) filters to nondescanned detectors (Olympus) and 483/32 (collagen by second harmonic generation) and 520/35 (GFP) filters to GASP detectors (Olympus). Typically, images from about 10 z planes, spaced 4 µm were collected every 45 seconds for up to one hour. We focused our new analysis of these existing movies on the GFP^{+} cells which are $CD74^{WT}$ skin DCs.

Statistics:

Statistical significance was calculated between two groups by Mann-Whitney test. Ordinary Mann-Whitney with multiple comparison was used to calculate statistical significance between multiple groups. Analyses were performed using GraphPad Prism 8 software.

Figure 1: **cell deformation of DCs leads to CCR7 upregulation.**

(**a**) Montage of the supplementary movie 1. An example of migrating CD11c-GFP DCs imaged by intravital microscopy in the ear dermis. Arrow indicates observed thinning events experienced by the cell while migrating. Upper panel: montage of the cd11c GFP cells with collagen incrementing 5 time points. Lower panel: montage of only the GFP channel (cd11c cells) with the same settings. Right part: zoom on one cell passing a thinning of around 3 µm. Scale bar 10 µm (**b**) Upper panel: Schematic representation of cells in the different conditions of confinement (Created with BioRender.com). Lower panel: Representative images of live immature dendritic cells (DCs) expressing LifeAct-GFP (grey) stained with NucBlue (DNA, red) under different conditions of confinement from left to right: non-confined (NC), confined at 4 µm height, confined at 3 µm height. (**c**) Representative images of live immature DCs expressing CCR7-GFPunder confinement of 4 and 3 µm heights at different time points of confinement. Top Images of transmission light (Trans) in grey and CCR7-GFP in green, lower images are GFP channel using false colors to better show differences in intensity (Min=0 Max=255). (**d**) Quantification of total GFP intensity in DCs under confinement of different conditions at different time points. Violin plot (medianand quartiles) representation where each dot is a cell. Outliers were calculated using prism ROUT test(Q=1%) and represented in grey. Left panel: GFP intensity at 30 minutes of confinement: N=4, n= 348 cells in 4 µm (82% of cells), n=314 cells in 3 µm (80% of cells). Middle panel: GFP intensity at 4 hours of confinement; N=4, n= 201 cells in in 4 µm (80% of cells), n=206 cells in 3 µm (86% of cells). Right panel: GFP intensity at 6 hours of confinement: N=4 n= 215 cells in in 4 µm, n=187 cells in 3 µm. P valueMann-Whitney test ****: p <0.0001. (**e**) Left panel: Representative immunofluorescence images of immature DCs confined for 4 hours at 4 and 3 µm. After removing the confinement, CCR7 was visualized using immunostaining (in grey) and the nucleus stained with Dapi (in red). Scale bar of 5 µm.Right panel: Quantification of CCR7 mean intensity after 4 hours of confinement, box plot representation where each dot is a cell. N=2, n=74 cells in 4 µm, n=89 cells in 3 µm, P value Mann- Whitney test ****: p <0.0001. (**f**) RT-qPCR data reveals the upregulation of *Ccr7* gene upon 4 hours ofconfinement with different heights. Graph: mean with SD of *Ccr7* fold change after normalization to non-confined immature cells. Each dot represents one experiment calculated as described in the methods. N=3, P value ordinary one-way ANOVA test ****: p <0.0001. (**g**) RT-qPCR data reveals the upregulation of *Ccr7* gene upon 30 minutes of confinement with different heights. Cells were left in the incubator for 4 hours after confinement was removed, and then collected for qPCR. Mean with SDof *Ccr7* fold change after normalization to non-confined control cells. Each dot represents oneexperiment calculated as described in the methods. N=2, P value ordinary one-way ANOVA test **: p=0.0021 (A-C), **: p=0.0052 (B-C). (**h-i**) Chemotactic response of live immature DCs under confinement of 4 and 3 µm heights to CCL19 gradient, representative of

2 independent experiments, n= 33 cells in 4 µm n= 43 cells in 3 µm. (**h**) Left panel: Picture of cells' trajectories under confinement in areas close to the chemokines gradient (gradient from right to left). In blue cells under 4 µm height, in orange cellsunder 3 µm height. Scale bar 100 µm. Middle panel: Representation of global steps taken by the cells under confinement with CCL19 gradient. The center of the 3 µm cells' tracks shifted towards the rightindicating an increase in their directionality towards the gradient. (**i**) Quantification of mean track speed of cells under confinement close to CCL19 gradient, box plot representation where each dot is a cell, P value Mann-Whitney test ****: p <0,0001.

Figure 2: **CCR7 upregulation in response to cell deformation depends on the activity of $cPLA_2$ and the integrity of the nuclear envelope**

(**a**) Left panel: Nucleus of live cells represented in different axes. Scale bar 3 µm. Right panel: Quantification of the nucleus projected area of live cells under confinement, box plot representation where each plot is a cell. N=2, n=71 cells in NC, n=70 cells in 4 µm, n=63 cells in 3 µm, P value ordinary one-way ANOVA test p <0.0001. (**b**) Total GFP intensity quantification in DCs from CCR7-GFP mice in confinement of 3 µm height after treatment with $cPLA_2$ inhibitor AACOF3 (25 µM) or ethanol as a control. Violin plot (median and quartiles) where each dot is a cell. Outliers were calculated using prism ROUT test (Q=1%) and represented in grey. N=3, n=393 cells in control n=163 cells in AACOF3 treated, P value Mann-Whitneytest ***: p <0,0001. (**c**) Quantification of total GFP intensity in DCs from CCR7-GFP mice after knock down of $cPLA_2$ (or control) by si-RNA in confinement of 4 hours at the heights of 4 and 3 µm. Violin plot (median and quartiles) each dot is a cell, N=2, n= 25 cells in 4 µm si-ctrl (80% of cells), n=21 cells in 4 µm si-$cPLA_2$ (75% of cells), n= 16 cells in 3 µm si-ctrl (75% of cells), n=16 cells in 3 µm si-$cPLA_2$ (76%of cells), P value ANOVA test **: p= 0,0059 (A-C), P= 0,0039. (**d**) Left panel: Representative immunofluorescence images of immature DCs from *Lmn A/C* wild type or knockout mice that were confined for 4 hours at the height of 3 µm. CCR7 was visualized using immunostaining (in grey) and thenucleus stained with Dapi (in red). Scale bar of 10 µm. Right panel: Quantification of CCR7 mean intensity signal after 4 hours of confinement, box plot representation where each dot is a cell. N=2, n=54 cells in Lmn A/C WT, n=60 cells in Lmn A/C KO, P value one-way ANOVA test ****: p <0.0001. (**e**)Left part: representative images of live immature DCs after NLS-GFP viral transduction (GFP signal in grey) to visualize nuclear envelope rupture in response to confinement at the heights of 4, 3, and 2 µm. Yellow stars were drawn to indicate the rupture and repair event. Right part: quantification of percentage of DCs displaying rupture events during the first hour of confinement with different heightsN=2. (**f**) Left part: representative immunofluorescence images of immature DCs that were either non-confined or confined for 4 hours at the heights of 4,3, and 2 µm. Lmn A/C was visualized using immunostaining (in grey) and the nucleusstained with Dapi (in red). Scale bar of 10 µm. Right part: Quantification of Lmn A/C mean intensity. Box plot representation where each dot is a cell. N=3, n=136 cells in non-confined, n=83 cells in 4 µm,n=81 cells in 3 µm, n=126 cells in 2 µm, P value Mann-Whitney test p <0.0001.

(**g**) RT-qPCR data reveals the upregulation of *Ccr7* gene upon 4 hours of confinement with different heights. Graph: mean with SD of *ccr7* fold change after normalization to non-confined controlcells. Each dot represents one experiment calculated as described in the methods. N=2, P value ordinary one-way ANOVA test **: p =0.0021, ****: p <0.0001.

(**h**) Left part: representative immunofluorescence images of immature DCs confined for 4 hours at the heights of 4,3, and 2 µm. $cPLA_2$ was visualized using immunostaining (in grey) and the nucleus stained with Dapi (in red). Scale bar of 10 µm. Right part: Quantification of $cPLA_2$ mean intensity, box plot representation where each dot is a cell. N=3, n=165 cells in 4 µm, n=178 cells in 3 µm, n=230 cells in 2 µm, P value Mann-Whitney test ****: p <0.0001 (**i**) Left part: representative immunofluorescence images of immature DCs from Lmn A/C WT and KO mice. Cells were confined for 4 hours at the height of 3 µm. $cPLA_2$ was visualized using immunostaining (in grey) and the nucleus stained with Dapi (in red). Scale bar of 5 µm. Right part: Quantification of $cPLA_2$ mean intensity, box plot representation where each dot is a cell. N=2, n=141 cells in WT, n=144 cells in KO, P value unpaired t-test p <0,0001.

Figure 3: **Arp2/3 tunes the $cPLA_2$ cell-shape sensitive response of dendritic cells**

(**a**) *Ccr7* gene expression upon 4 hours of confinement in cells treated with CK666 (25µM) or DMSO and confined at the height of 3 µm, measured by RT-qPCR. Mean with SD of *Ccr7* fold change after normalization to non-confined control cells. Each dot represents one experiment calculated as described in the methods. N=2, P value ordinary one-way ANOVA test ****: p <0.0001, ***: p =0.0001. (**b**) Left part: representative immunofluorescence images of immature DCs treated either with CK666 (25 µM) or DMSO and confined for 4 hours at the height of 3 µm. $cPLA_2$ was visualized using immunostaining (in grey) and the nucleus stained with Dapi (in red). Scale bar of 5 µm. Right part: Quantification of $cPLA_2$ mean intensity, box plot representation where each dot is a cell. N=2, n=121 cells in control condition, n=64 cells in CK treated condition, P value Mann-Whitney test p <0.0001. (**c**) Left part: representative immunofluorescence images of immature DCs from WASP WT and KO that were confined for 4 hours at the height of 3 µm. CCR7 was visualized using immunostaining (in grey), the nucleus stained with Dapi (in red) and actin stained with phalloidin (in green). Scale bar of 10 µm. Rightpart: graph: quantification of CCR7 mean intensity, box plot representation where each dot is a cell. N=2, n=70 cells in WT, n=38 cells in KO, P value unpaired t-test p <0.0001. (**d**) RT-qPCR data of *Ccr7* gene expression upon 4 hours of confinement in cells from $Arpin^{WT}$ or $Apin^{KO}$mice that were confined at the heights of 4, and 3 µm. Graph represents mean with SD of *Ccr7* fold change after normalization to non-confined control cells. Each dot represents one experiment calculated as described in the methods. N=2, P values ordinary one-way ANOVA test ***: p = 0.0002, **: p= 0.0015. (**e**) Left part: representative immunofluorescence images of immature DCs from Arpin WT and KO confined for 4 hours at the heights of 4 and 3 µm. $cPLA_2$ was visualized using immunostaining (in grey) and the nucleus stained with Dapi (in red). Scale bar of 5 µm. Right part: Quantification of $cPLA_2$ mean intensity, box plot representation where each dot is a cell. N=2, n=59 cells in WT 4 µm, n=87 cells in

KO 4 µm, n=75 cells in WT 3 µm, P value ordinary one-way ANOVA test****: p <0.0001, **: P= 0.0043. (**f**) RT-qPCR data of *Ccr7* gene expression upon 4 hours of confinementin cells from Arpin^{WT} or Apin^{KO} that have been knocked down for cPLA$_2$ and confined at the heights of 4, and 3 µm. Graph: represents mean with SD of *Ccr7* fold change after normalization to non-confined control cells. Each dot represents one experiment calculated as described in the methods. N=2, P values ordinary one-way ANOVA test **: p = 0.0046 (B-C), **: p= 0.0080. (**g**) Left part: representative images of live immature dendritic cells (DCs) from Arpin^{WT} or Apin^{KO} mice expressing LifeAct-GFP (grey) stained with NucBlue (DNA, red) under confinement of 4 and 3 µm heights, represented in different axes. Yellow stars indicating the actin cloud near the nuclear are in WT cells at 3 µm and KO cells at 4 µm. Right part: Quantification of LifeAct nuclear to cytosolic ratio calculatedas explained in supplementary figure 2. N=2, n=55 cells in WT 4 µm, n=33 cells in KO 4 µm, n=70 cells in WT 3 µm, P value ordinary one-way ANOVA test ****: p <0.0001, ***: p=0.0001.

Figure 4: **Increased homeostatic migration in Arpin^{KO} from skin to lymph nodes**

(**a**) Gating strategy to characterize dendritic cells in the skin- draining lymph nodes of Arpin^{WT} and Arpin^{KO} mice at steady-state conditions. Example of Arpin^{WT} mouse: after gating on live cells, immune cells were CD45 high, from there gating on CD11c and MHCII was done to differentiate resident DCs (MHCII low, CD11c high) and migratory DCs (MHCII high, CD11c high). On the migratory DCs population (CD11b high, CD103 low) cells were the migratory cDCs in which (CD11b high, EPCAM low) were characteristic of the migratory DC2. On the resident DCs population (MHCII low, CD11c low) CD11b low, CD8a high DCs were characteristic of the resident DC2. (**b**) Plots of normalized number of migratory cDC2 in the skin draining lymph nodes of Arpin^{WT} (*flox/flox cre-/-*) and KO (*flox/flox cre+/-*) mice, N=3 where each dot is a mouse. P value Mann-Whitney test *: p= 0,0400, ns: not-significant. (**c**) Gating strategy used to characterize dendritic cells in the skin of Arpin^{WT} or Apin^{KO} mice at steady-state conditions. Example of Arpin^{WT} mouse: after gating on live cells, immune cells were CD45 high, MHCII high, CD11c high were DC population, among them (CD11b high, CD103 low) were the migratory DCs, from this population (CD11b high EPCAM low) were characteristic of the migratory cDC2. (**d**) Plots of normalized number of cDC2 in the skin draining lymph nodes of Arpin^{WT} or Apin^{KO} mice, N=3 where each dot is a mouse. P value Mann-Whitney test, ns: not-significant. (**e**) Histograms of FACS analysis on the expression of CCR7 by LPS-DCs from Arpin^{WT} and Arpin^{KO} mice, representative example of 2 independent experiments. (**f**) Picture of cells' trajectories of LPS-bone marrow derived DCs from Arpin^{WT} or Apin^{KO} mice moving in collagen gels of 3ng/ml density in response to gradient of CCL19. (**g**) Analysis of directionality of these cells in the gel with and without the gradient showing no differencebetween the WT and KO of Arpin. (**h**) Analysis of cells speed in the gel with and without the gradient of CCL19 demonstrating decrease in speed in LPS activated cells from Arpin$^{WT/KO}$. N=2,

n=400 cells in Arpin^{WT} without chemokine, n=485 cells in Arpin^{WT} with chemokine, n=470 cells in Arpin^{KO} without chemokine, n=468 cells in Arpin^{KO} with chemokine.

Figure 5: **cPLA$_2$ mediates *Ccr7* upregulation through activity of *Ikk*β**

(**a**) RT-qPCR data of *Ccr7* gene expression upon 4 hours of confinement in cells treated with Ikkβ inhibitor BI605906 (30 µM) or with DMSO and were confined at the height of 3 µm. Graph: represents mean with SD of *Ccr7* fold change after normalization to non-confined control cells. Each dot represents one experiment calculated as described in the methods. N=2, P values ordinary one- way ANOVA test ****: p<0.0001, *: p= 0.0134. (**b**) RT-qPCR data of *Ccr7* gene expression upon 4 hoursof confinement in cells from *Ikbkb* ^{WT} or *Ikbkb* ^{KO} mice that were confined at the height of 3 µm. Graph: represents mean with SD of *Ccr7* fold change after normalization to non-confined control cells.Each dot represents one experiment calculated as described in the methods. N=2, P values ordinary one-way ANOVA test ****: p<0.0001, ***: p= 0.0001, ns: not-significant. (**c**) Left part: representative immunofluorescence images of immature DCs knocked down or not for cPLA$_2$ that were confined for 4 hours at the heights of 4 and 3 µm. NFκB (P65) was visualized using immunostaining (in grey) and the nucleus stained with Dapi (in red) and phalloidin (in green). Scale bar of 10 µm. Right part: Quantification of NFκB (P65) mean intensity, box plot representation where each dot is a cell. N=2, n=24 cells in si-control confined at 4 µm, n=60 cells si-cPLA$_2$ confined at 4 µm, n=60 cells si-control and si-cPLA$_2$ confined at 3 µm, P value unpaired t-test ****: p <0.0001, ns= not-significant. (**d**) Left part: representative immunofluorescence images of immature DCs treated with Ikkβ inhibitor BI605906 (30 µM) or with DMSO and confined for 4 hours at the height of 3 µm. cPLA$_2$ was visualized using immunostaining (in grey) and the nucleus stained with Dapi (in red). Scale bar of 5 µm. right part: Quantification of cPLA$_2$ mean intensity, box plot representation where each dot is a cell. N=2, n=29 cells in DMSO, n=23 cells in BI605906, P values ordinary one-way ANOVA test ns: not-significant.

Figure 6: **A cPLA$_2$-dependent transcriptional program regulates DCs regulatory properties**

(**a-h**) Data from bulk RNA-seq analysis on BMDCs from cPLA$_2$ WT and cPLA$_2$ KO mice (**a**) Heat map of all the differentially expressed genes in cPLA^{WT} and cPLA^{KO} cells in their immature non-confined condition or immature confined at 3 µm-height. (**b**)Principal-component analysis (PCA) of the bulk RNA-Seq samples. ThePCA figure represents a two-dimensional scatterplot of the first two principal components of the RNA- Seq data. Sample groups at different confinement conditions are represented by different forms. Eachdot represents a biological replicate of an RNA-Seq sample. (**c**) Venn diagram describing the differentially expressed genes between cPLA^{WT} and cPLA^{KO} cells in response to confinement after normalization to the non-confined conditions using as this threshold: p value < = 0.05 and fold-change > = 1.5. (**d**) Bubble plot of some Reactom pathway

enrichment analysis on the genes upregulated in $cPLA^{WT}$. The size of the bubble represents the number of genes in each pathway. The pathway term is displayed in Y axis, -log10 (p) is displayed in X axis. (**e**) Fragments Per Kilobase of transcript per Million mapped reads of *Ccr7* gene in the different condition of the bulk RNA-seq experiment with each color of the triplicate samples representing one condition. (**f**) Heat map of some genes moving with *Ccr7* (upregulated in $cPLA_2^{WT}$ and down regulatedin $cPLA_2^{KO}$). (**g**) Heat map of IFN-related genes that are upregulated in $cPLA^{WT}$ and down regulated in $cPLA^{KO}$. (**h**) Heatmap of innate sensing-related genes in $cPLA_2^{WT}$ and $cPLA_2^{KO}$ cells.

Figure 7: The $cPLA_2$-dependent cell-shape sensitive program shapes the immune phenotype of DCs

(**a**) Heat map of the differentially expressed genes in $cPLA_2^{WT}$ and $cPLA_2^{KO}$ cells treated or not with LPS. (**b**) Venn diagram describing the differentially expressed genes between 3 µm-confined and LPS DCs. (**c**) Heat map of some $cPLA_2$-related genes, $cPLA_2$ gene (*Pla2g4a*) in red. (**d**) Bubble plot of some Reactom enrichment analysis on the significantly upregulated pathways in LPS condition. (**e**) Bubble plot of some Reactom enrichment analysis on the significantly upregulated pathways in confinement condition. (**f**) Heat map of the genes in the NFκB- related pathways found in **d** (upper genes in dark orange) and in **e** (lowers genes in light orange). (**g**) FACS analysis of some immune-activating genes between DCs activated with LPS or confined at 3 µm height. Graphs showing geometric mean intensity of CD80, CD86, and MHCII. Mean with SEM, N=3 each condition was done in duplicates, each dot is the mean of one independent experiment. (**h**) Antigen presentation assays of OT-II (CD4) T-cells incubated with DCs either activated with LPS or confined at 3 µm. Left panel: percentage of $CD69^+$ $CD4^+$ OT-II T cells in live cells after 18 h of incubation with OVA peptide II and pre-incubated with 3 µm confined or LPS-DCs. Right panel: Percentage of CFSE− $CD4^+$ OT-II T cells in live cells after 3 days of incubation with OVA peptide II and pre-incubattion with 3 µm confined or LPS-DCs, analyzed by flow cytometry. Graph: Mean ±SEM, N=5, P values multiple t-test, ***: $p = 0.0001$, ****: $p < 0.0001$.

Supplementary figures:

Figure S1: **GFP quantification approach**

(**a**) Quantification approach to quantify GFP intensity in each cells. (**b**) representative images of immature DCs confined for 4 hours at the height of 3 µm from C57BL/6J (WT) or GFP/GFP mice, CCR7was visualized using immunostaining (in orange) and the nucleus stained with Dapi (in cyan) scale bar10 µm.

Figure S2: cPLA$_2$ activity is not necessary for LPS-induced *Ccr7* up regulation upon confinement

(a) RT-qPCR data of cPLA$_2$ gene expression upon knock down of cPLA$_2$ with Si-RNA technique, N=3. **(b)** FACS analysis of CCR7 expression in DCs treated or not with cPLA$_2$ inhibitor AACOF3 (25 µM) after activation with LPS as described in the methods, immature DCs were taken as a control, representativeof 2 independent experiments. (**c**) RT-qPCR data of *Ccr7* gene expression in cells knocked down or notfor cPLA$_2$ and activated with LPS, data shows no difference in *Ccr7* up regulation in response to LPS in both cells types. N=2. (**d**) Left part: Representative images LAP2B-GFP transduced immature DCs underconfinement of 3 µm-height with non-confined cells as control. Right part: quantification of the meansquare displacement of the nuclear envelope of DCs under the previous conditions calculated as explained in the methods. N=3, each dot is a cell, n=34 cells in non-confined, n=51 cells in 3 µm. (**e**) RT-qPCR data of *Ccr7* gene expression in cells confined at 2 µm height and cells activated with LPS after confinement at 2 µm height, N=2. (**f**) Quantification approach of LifeAct-GFP intensity in live cells underconfinement: 1- choose Z-stack lower plan (since cells don't always touch the upper plan). 2- optical section at the surface cortex. 3-Segmentation to define cell and nuclear contour at the surface. 4- Measurement of LifeAct-GFP ratio: Actin Ratio= Nuclear surface mean actin intensity/cell surface meanactin intensity (ratio <1 => actin is mostly cortical).

Figure S3: **Bulk RNA-seq analysis shows major transcriptional changes in cells in response to confinement in a cPLA$_2$-dependent manner**

(**a**) Volcano plot representing all the differentially expressed genes in two different comparisons, in grey are the genes that have the same level of expression in both conditions, in red are the genes upregulated, and in blue are the genes down regulated. left part: illustration of the gens in LPS-DCs from cPLA$_2^{WT}$ and cPLA$_2^{KO}$ mice. Right part: illustration of the gens in confined-DCs from cPLA $_2^{WT}$ and cPLA $_2^{KO}$ mice. (**b**) Heat map of some cytokines gens in DCs in response to confinement at 3 µm-height or LPS stimulation (**c**) Upper part: heat map of some cytokines' expression by LPS or confined DCs. Lower part: cytokine secretion analysis by luminex of the same cytokines showing their protein level

of expression in the supernatant of LPS or confined DCs 48 hours after the confinement or the LPS activation. N=5 (**d**) FACS analysis on percentage of live CD11c high dendritic cells shows no difference between cells either activated with LPS or confined at 3 µm in the same presentation assay experiments showed in figure 6. Graph: mean with SEM, N=2 (**e**) MLR: mixed lymphocyte reaction analysis: dendritic cells were confined for 4 hours at 3 µm then recovered or activated with LPS and then incubated with allogeneic CD3+ T cells at different T: dendritic cell (DC) ratios for4 d. T-cell proliferation (mean + SEM) was measured by CFSE uptake. N=2.

Supplementary movies:

Movie S1: 2 photon movie of cd11c YFP DCs in mouse ear skin.

Example of a cd11c-GFP DCs in green migrating in ear dermis with collagen fibers observed in grey. The contour of the cells is shown in pink and arrows appear to indicate thinning events experienced by the cell while migrating. These thinning events could range in size from 2 to 5 µm. Time interval of 45 seconds and scale bar is 20 µm.

Movie S2: Movie of BMDCs from CCR7/GFP mice under confinement.

Bone marrow derived dendritic cells from CCR7/GFP mice under confinement of 4 and 3 µm height.

Upper part is the images of cells in transmission light (in grey) and GFP signal (in green). Lower part isthe GFP signal using false colors (Physics LUT). The warmer the color the more the intensity of GFP signal. The transmission images were corrected for bleach (with the function bleach correction in ImageJ), GFP signal was smoothed using the Median filter. Time is showed in minutes (using time stamper function). Movie created with ImageJ software [67]

Movie S3: Movie of BMDCs transduced with NLS-GFP under confinement of 2 µm height.

Example of NLS-GFP expression in BMDCs under 2 µm height. The movie shows examples from 2 different positions of the same condition displaying rupture (when the GFP signal is diffused) and repair(when the signal is concentrated in the nucleus) events. The stacks were merged using the stack-mergefunction with ImageJ software. The movie is a Max Z projection of the GFP signal. Time is showed in minutes (using time stamper function).

Movie S4: Movie of live BMDCs expressing LifeAct/GFP under confinement of 4 µm height.

Example of Arpin^{WT} and Arpin^{KO} DCs expressing LifeAct/GFP under 4 µm height and stained with NucBlue to visualize the nucleus (DNA). Movies in Z-stack of 10 steps (step size of 0.33 µm). Upper partand lower part are Arpin^{WT} and Arpin^{KO} respectively. Left part is Nucleus channel, middle part is LifeAct/GFP channel, and right part is merge of both previous channels. Scale bar of 5 µm. Arrows drawn by hand to show the actin patch observed close to the nuclear area only in Arpin^{KO} DC.

References

1. *Dendritic cells: specialized and regulated antigen processing machines.* **Mellman I, Steinman RM.** 2001, Cell.

2. *The priming of helper T cells.* **CA, Janeway Jr.** 1989, Semin Immunol.

3. *Dendritic cells: translating innate to adaptive immunity.* **Steinman RM, Hemmi H.** 2006, Curr Top Microbiol Immunol.

4. *Mechanisms and consequences of dendritic cell migration.* **Alvarez D, Vollmann EH, von Andrian UH.** 2008, Immunity.

5. *Dendritic cell migration in health and disease.* **Worbs T, Hammerschmidt SI, Förster R.** 2017, Nat Rev Immunol.

6. *Homeostatic NF-κB Signaling in Steady-State Migratory Dendritic Cells Regulates Immune Homeostasis and Tolerance.* **Baratin M, Foray C, Demaria O, Habbeddine M, Pollet E, Maurizio J, Verthuy C, Davanture S, Azukizawa H, Flores-Langarica A, Dalod M, Lawrence T.** 2015, Immunity.

7. *CCR7 and its Ligands: Balancing Immunity and Tolerance.* **Förster, R., Davalos-Misslitz, A. C., and Rot, A.** 2008, Nat. Rev. Immunol.

8. *Interstitial dendritic cell guidance by haptotactic chemokine gradients.* **Weber M, Hauschild R, Schwarz J, Moussion C, de Vries I, Legler DF, Luther SA, Bollenbach T, Sixt M.** 2013, Science.

9. *Dendritic Cells and the Control of Immunity.* **Banchereau, J., and Steinman, R. M.** 1998, Nature.

10. *Pathogen Recognition by the Innate Immune System.* **Himanshu Kumar, Taro Kawai & Shizuo Akira.** 2011, International Reviews of Immunology.

11. *New Insights of CCR7 Signaling in Dendritic Cell Migration and Inflammatory Diseases.* **Hong W, Yang B, He Q, Wang J, Weng Q.** 2022, Front Pharmacol.

12. *ATP promotes the fast migration of dendritic cells through the activity of pannexin 1 channels and P2X7 receptors.* **Sáez PJ, Vargas P, Shoji KF, Harcha PA, Lennon-Duménil AM, Sáez JC.** 2017, Sci Signal.

13. *Autocrine/paracrine TGF-β1 inhibits Langerhans cell migration.* **Aleh Bobr, Botond Z. Igyarto, Krystal M. Haley , Ming O. Li, Richard A. Flavell, and Daniel H. Kaplan.** 2012, PNAS.

14. *Prostaglandin E2 is a key factor for CCR7 surface expression and migration of monocyte-derived dendritic cells.* **Scandella E, Men Y, Gillessen S, Förster R, Groettrup M.** 2002, Blood.

15. *CCL19/CCL21-triggered signal transduction and migration of dendritic cells requires prostaglandin E2.* **Scandella E, Men Y, Legler DF, Gillessen S, Prikler L, Ludewig B, Groettrup M.** 2004, Bllod.

16. *Migratory dermal dendritic cells act as rapid sensors of protozoan parasites.* **Ng LG, Hsu A, Mandell MA, Roediger B, Hoeller C, Mrass P, Iparraguirre A, Cavanagh LL, Triccas JA, Beverley SM, Scott P, Weninger W.** 2008, PLoS Pathog.

17. *Luminal bacteria recruit CD103+ dendritic cells into the intestinal epithelium to sample bacterial antigens for presentation.* **Farache J, Koren I, Milo I, Gurevich I, Kim KW, Zigmond E, Furtado GC, Lira SA, Shakhar G.** 2013, Immunity.

18. *Control of Mechanotransduction by Molecular Clutch Dynamics.* **Elosegui-Artola A, Trepat X, Roca-Cusachs P.** 2018, Trends Cell Biol.

19. *Compromised nuclear envelope integrity drives TREX1-dependent DNA damage and tumor cell invasion.* **Nader GPF., Agüera-Gonzalez S, Routet F, Gratia M, Maurin M, Cancila V, Cadart C, Palamidessi A, Ramos RN, San Roman M, Gentili M, Yamada A, Williart A, Lodillinsky C, Lagoutte E, Villard C, Viovy JL, Tripodo C, Galon J, Scita G, Manel N, Chavrier P, Piel.** 2021, Cell.

20. *Emerging modes of collective cell migration induced by geometrical constraints.* **Vedula SR, Leong MC, Lai TL, Hersen P, Kabla AJ, Lim CT, Ladoux B.** 2012, Proc Natl Acad Sci U S A.

21. *Perinuclear Arp2/3-driven actin polymerization enables nuclear deformation to facilitate cell migration through complex environments.* **Thiam HR, Vargas P, Carpi N, Crespo CL, Raab M, Terriac E, King MC, Jacobelli J, Alberts AS, Stradal T, Lennon-Dumenil AM, Piel M.** 2016, Nat Commun.

22. *Editorial: Immune Cell Migration in Health and Disease.* **Renkawitz J, Donnadieu E, Moreau HD.** 2022, Front Immunol.

23. *SCRT III repairs nuclear envelope ruptures during cell migration to limit DNA damage and cell death.* **Raab M, Gentili M, de Belly H, Thiam HR, Vargas P, Jimenez AJ, Lautenschlaeger F, Voituriez R, Lennon-Duménil AM, Manel N, Piel M.** 2016, Science.

24. *A close-up view of migrating Langerhans cells in the skin.* **Patrizia Stoitzner, Hella Stössel, Nikolaus Romani, Kristian Pfaller,.** 1, s.l. : J Invest Dermatol., 2002, Vol. 118.

25. *The nucleus acts as a ruler tailoring cell responses to spatial constraints.* **Lomakin AJ, Cattin CJ, Cuvelier D, Alraies Z, Molina M, Nader GPF, Srivastava N, Sáez PJ, Garcia-Arcos JM, Zhitnyak IY, Bhargava A, Driscoll MK, Welf ES, Fiolka R, Petrie RJ, De Silva NS, González-Granado JM, Manel N, Lennon-Duménil AM, Müller DJ, Piel M.** 2020, Science.

26. *The Cell Nucleus Serves as a Mechanotransducer of Tissue Damage-Induced Inflammation.* **Balázs Enyedi, Mark Jelcic, Philipp Niethammer.** 2016, Cell.

27. *Intracellular calcium signals regulating cytosolic phospholipase A2 translocation to internal membranes.* **Evans JH, Spencer DM, Zweifach A, Leslie CC.** 2001, J Biol Chem.

28. *5-Lipoxygenase: mechanisms of regulation.* **Rådmark O, Samuelsson B.** 2009, J Lipid Res.

29. **Makoto Murakami, Yoshihito Nakatani, Hiroshi Kuwata, Ichiro Kudo.** Cellular components that functionally interact with signaling phospholipase A2. *Biochimica et Biophysica Acta (BBA) - Molecular and Cell Biology of Lipids.* 2000.

30. *Cytosolic phospholipase A2: physiological function and role in disease.* **C.Leslie, Christina.** 2015, Jornal of lipid research.

31. *The nucleus measures shape changes for cellular proprioception to control dynamic cell behavior.* **Venturini V, Pezzano F, Català Castro F, Häkkinen HM, Jiménez-Delgado S, Colomer-Rosell M, Marro M, Tolosa-Ramon Q, Paz-López S, Valverde MA, Weghuber J, Loza-Alvarez P, Krieg M, Wieser S, Ruprecht V.** 2020, Science.

32. *Nuclear positioning facilitates amoeboid migration along the path of least resistance.* **Jörg Renkawitz, Aglaja Kopf, Julian Stopp, Ingrid de Vries, Meghan K. Driscoll, Jack Merrin, Robert Hauschild, Erik S. Welf, Gaudenz Danuser, Reto Fiolka , Michael Sixt.** s.l. : Nature, 2019, Vol. 568.

33. *Confinement and low adhesion induce fast amoeboid migration of slow mesenchymal cells.* **Liu YJ, Le Berre M, Lautenschlaeger F, Maiuri P, Callan-Jones A, Heuzé M, Takaki T, Voituriez R, Piel M.** 2015, Cell.

34. *Actin flows mediate a universal coupling between cell speed and cell persistence.* **Paolo Maiuri, Jean-François Rupprecht, Stefan Wieser, Verena Ruprecht, Olivier Bénichou, Nicolas Carpi, Mathieu Coppey, Simon De Beco, Nir Gov, Carl-Philipp Heisenberg, Carolina Lage Crespo, Franziska Lautenschlaeger, Maël Le Berre, Ana-Maria Lennon-Dumen.** 2015, Cell.

35. *Generation of large numbers of dendritic cells from mouse bone marrow cultures supplemented with granulocyte/macrophage colony-stimulating factor.* **Inaba K, Inaba M, Romani N, Aya H, Deguchi M, Ikehara S, Muramatsu S, Steinman RM.** 1992, J Exp Med. .

36. *Analysis of the CCR7 expression on murine bone marrow-derived and spleen dendritic cells.* **Ritter U, Wiede F, Mielenz D, Kiafard Z, Zwirner J, Körner H.** 2004, J Leukoc Biol.

37. *Migratory properties of pulmonary dendritic cells are determined by their developmental lineage.* **Nakano H, Burgents JE, Nakano K, Whitehead GS, Cheong C, Bortner CD, Cook DN.** 2013, Mucosal Immunol.

38. *Collagen-based cell migration models in vitro and in vivo.* **Wolf K, Alexander S, Schacht V, Coussens LM, von Andrian UH, van Rheenen J, Deryugina E, Friedl P.** 8, s.l. : Semin Cell Dev Biol., 2009, Semin Cell Dev Biol., Vol. 20.

39. *Mechanisms of epithelial wound detection.* **Balázs Enyedi, Philipp Niethammer,.** 2015, Trends Cell Biol.

40. *C2 domain membrane penetration by group IVA cytosolic phospholipase A_2 induces membrane curvature changes.* **Ward KE, Ropa JP, Adu-Gyamfi E, Stahelin RV.** 2012, J Lipid Res.

41. *Nuclear deformations, from signaling to perturbation and damage.* **Nader GPF, Williart A, Piel M.** 2021, Curr Opin Cell Biol.

42. *Nuclear membrane stretch and its role in mechanotransduction.* **Enyedi B, Niethammer P.** 2017, Nucleus.

43. *Coordinated increase of nuclear tension and lamin-A with matrix stiffness outcompetes lamin-B receptor that favors soft tissue phenotypes.* **Buxboim A, Irianto J, Swift J, Athirasala A, Shin JW, Rehfeldt F, Discher DE.** 2017, Mol Biol Cell.

44. *Nuclear envelope breakdown requires overcoming the mechanical integrity of the nuclear lamina.* **Panorchan P, Schafer BW, Wirtz D, Tseng Y.** 2004, J Biol Chem.

45. *Demonstration of mechanical connections between integrins, cytoskeletal filaments, and nucleoplasm that stabilize nuclear structure.* **Andrew J. Maniotis, Christopher S. Chen, and Donald E. Ingber.** 1997, PNAS.

46. *Nuclear mechanics and mechanotransduction in health and disease.* **Isermann P, Lammerding J.** 2013, Curr Biol.

47. *The LINC complex transmits integrin-dependent tension to the nuclear lamina and represses epidermal differentiation.* **Carley E, Stewart RM, Zieman A, Jalilian I, King DE, Zubek A, Lin S, Horsley V, King MC.** 2021, Elife.

48. *Wiskott-Aldrich syndrome protein restricts cGAS/STING activation by dsDNA immune complexes.* **Piperno GM, Naseem A, Silvestrelli G, Amadio R, Caronni N, Cervantes-Luevano KE, Liv N, Klumperman J, Colliva A, Ali H, Graziano F, Benaroch P, Haecker H, Hanna RN, Benvenuti.** 2020, JCI Insight.

49. *Inhibitory signalling to the Arp2/3 complex steers cell migration.* **Dang I, Gorelik R, Sousa-Blin C, Derivery E, Guérin C, Linkner J, Nemethova M, Dumortier JG, Giger FA, Chipysheva TA, Ermilova VD, Vacher S, Campanacci V, Herrada I, Planson AG, Fetics S, Henriot V, David V, Oguievetskaia K, Lakisic G, Pierre F, Steffen A.** 2013, Nature.

50. *Arpin Regulates Migration Persistence by Interacting with Both Tankyrases and the Arp2/3 Complex.* **Simanov G, Dang I, Fokin AI, Oguievetskaia K, Campanacci V, Cherfils J, Gautreau AM.** 2021, Int J Mol Sci.

51. *Impaired dendritic-cell homing in vivo in the absence of Wiskott-Aldrich syndrome protein.* **Sofia de Noronha, Samantha Hardy, Joanna Sinclair, Michael P Blundell, Jessica Strid, Oliver Schulz, Jörg Zwirner, Gareth E Jones, David R Katz, Christine Kinnon, Adrian J Thrasher.** 2005, Blood.

52. *WASp triggers mechanosensitive actin patches to facilitate immune cell migration in dense tissues.* **Gaertner F, Reis-Rodrigues P, de Vries I, Hons M, Aguilera J, Riedl M, Leithner A, Tasciyan S, Kopf A, Merrin J, Zheden V, Kaufmann WA, Hauschild R, Sixt M.** 2022, Dev.Cell.

53. *Monocytes from Wiskott-Aldrich patients display reduced chemotaxis and lack of cell polarization in response to monocyte chemoattractant protein-1 and formyl-methionyl-leucyl-phenylalanine.* **Badolato, R., Sozzani, S., Malacarne, F., Bresciani, S., Fiorini, M., Borsatti, A., Albertini, A., Mantovani, A., Ugazio, A. G., & Notarangelo, L. D.** 1998, Journal of immunology.

54. *Homeostatic IL-13 in healthy skin directs dendritic cell differentiation to promote TH2 and inhibit TH17 cell polarization.* **Mayer, J.U., Hilligan, K.L., Chandler, J.S. et al.** 2021, Nat Immunol.

55. *Minimal differentiation of classical monocytes as they survey steady-state tissues and transport antigen to lymph nodes.* **Jakubzick C, Gautier EL, Gibbings SL, Sojka DK, Schlitzer A, Johnson TE, Ivanov S, Duan Q, Bala S, Condon T, van Rooijen N, Grainger JR, Belkaid Y, Ma'ayan A, Riches DW, Yokoyama WM, Ginhoux F, Henson PM, Randolph GJ.** 3, s.l. : Immunity, 2013, Vol. 39.

56. *The tumor microenvironment.* **Anderson NM, Simon MC.** 2020 , Curr Biol. .

57. *A conserved dendritic-cell regulatory program limits antitumour Immunity.* **Maier B, Leader AM, Chen ST, Tung N, Chang C, LeBerichel J, Chudnovskiy A, Maskey S, Walker L, Finnigan JP, Kirkling ME, Reizis B, Ghosh S, D'Amore NR, Bhardwaj N, Rothlin CV, Wolf A, Flores R, Marron T, Rahman AH, Kenigsberg E, Brown BD, Merad M.** 2020, Nature.

58. *CCR7 and IRF4-dependent dendritic cells regulate lymphatic collecting vessel permeability.* **Ivanov S, Scallan JP, Kim KW, Werth K, Johnson MW, Saunders BT, Wang PL, Kuan EL, Straub AC, Ouhachi M, Weinstein EG, Williams JW, Briseño C, Colonna M, Isakson BE, Gautier EL, Förster R, Davis MJ, Zinselmeyer BH, Randolph GJ.** 2016, J Clin Invest.

59. *CCR7 mediates human breast cancer cell invasion, migration by inducing epithelial–mesenchymal transition and suppressing apoptosis through AKT pathway.* **Xu B, Zhou M, Qiu W, Ye J, Feng Q.** 2017, Cancer Med.

60. *CCR7: Roles in cancer cell dissemination, migration and metastasis formation.* **Daniel F.Legler, EdithUetz-von Allmen, Mark A.Hauser.** 2014, The International Journal of Biochemistry & Cell Biology.

61. *GM-CSF Mouse Bone Marrow Cultures Comprise a Heterogeneous Population of CD11c(+)MHCII(+) Macrophages and Dendritic Cells.* **Helft J, Böttcher J, Chakravarty P, Zelenay S, Huotari J, Schraml BU, Goubau D, Reis e Sousa C.** 2015, Immunity.

62. *Physical limits of cell migration: control by ECM space and nuclear deformation and tuning by proteolysis and traction force.* **Wolf K, Te Lindert M, Krause M, Alexander S, Te Riet J, Willis AL, Hoffman RM, Figdor CG, Weiss SJ, Friedl P.** 2013, J Cell Biol. .

63. *Globally optimal stitching of tiled 3D microscopic image acquisitions. .* **Preibisch S, Saalfeld S, Tomancak P.** 2009, Bioinformatics.

64. *The first World Cell Race.* **Maiuri P, Terriac E, Paul-Gilloteaux P, Vignaud T, McNally K, Onuffer J, Thorn K, Nguyen PA, Georgoulia N, Soong D, Jayo A, Beil N, Beneke J, Lim JC, Sim CP, Chu YS and WCR participants, Jiménez-Dalmaroni A, Joanny JF, Thiery JP, Erfle H, Parsons M, Mitchiso.** 2012, Curr Biol. .

65. *Image Processing with ImageJ.* **Abramoff, M.D., Magalhaes, P.J., Ram, S.J.** 2004, Biophotonics International, pp. 36-42.

66. *WebGestalt 2019: gene set analysis toolkit with revamped UIs and APIs.* **Liao Y, Wang J, Jaehnig EJ, Shi Z, Zhang B.** 2019, Nucleic Acids Res.

Figure 1

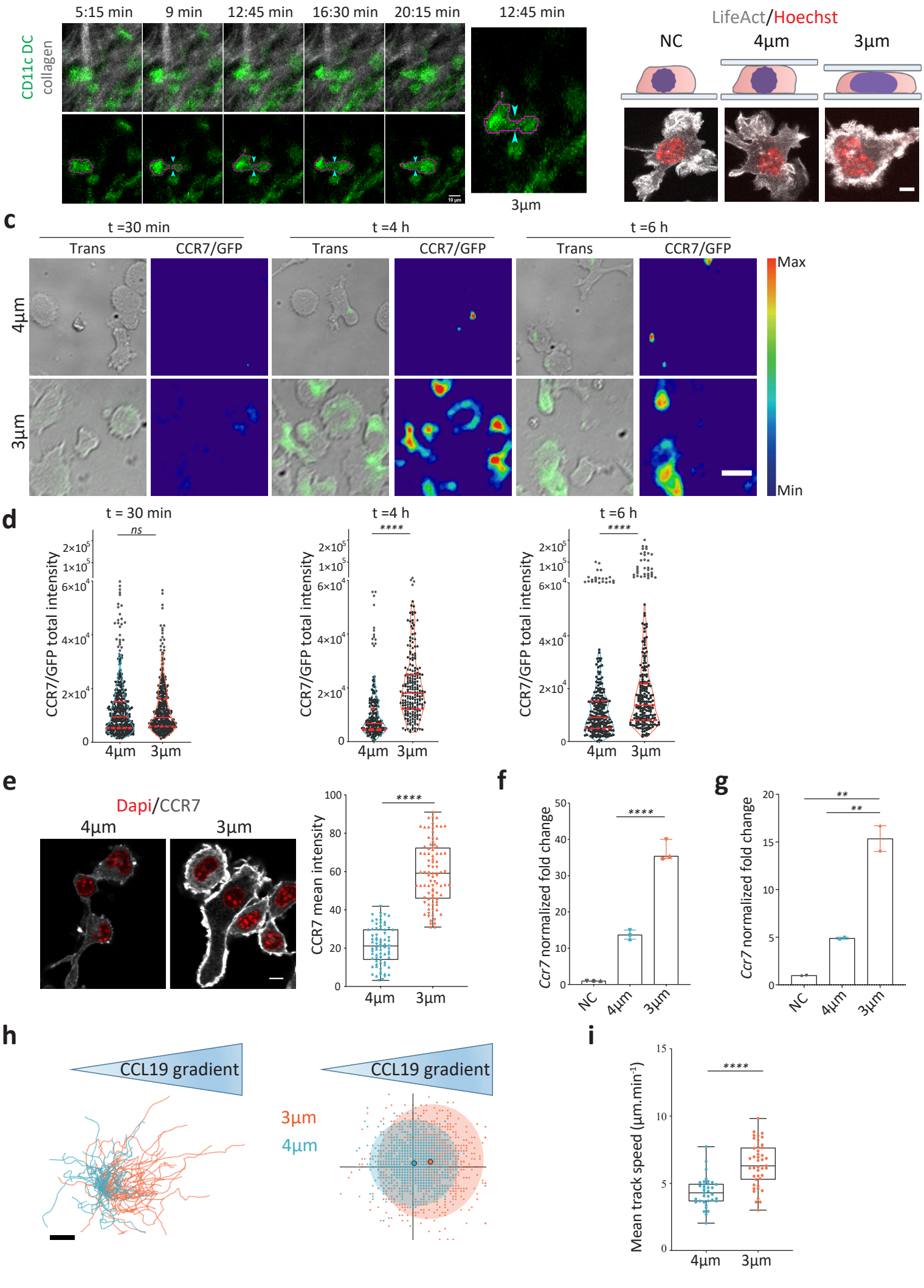

Figure 2

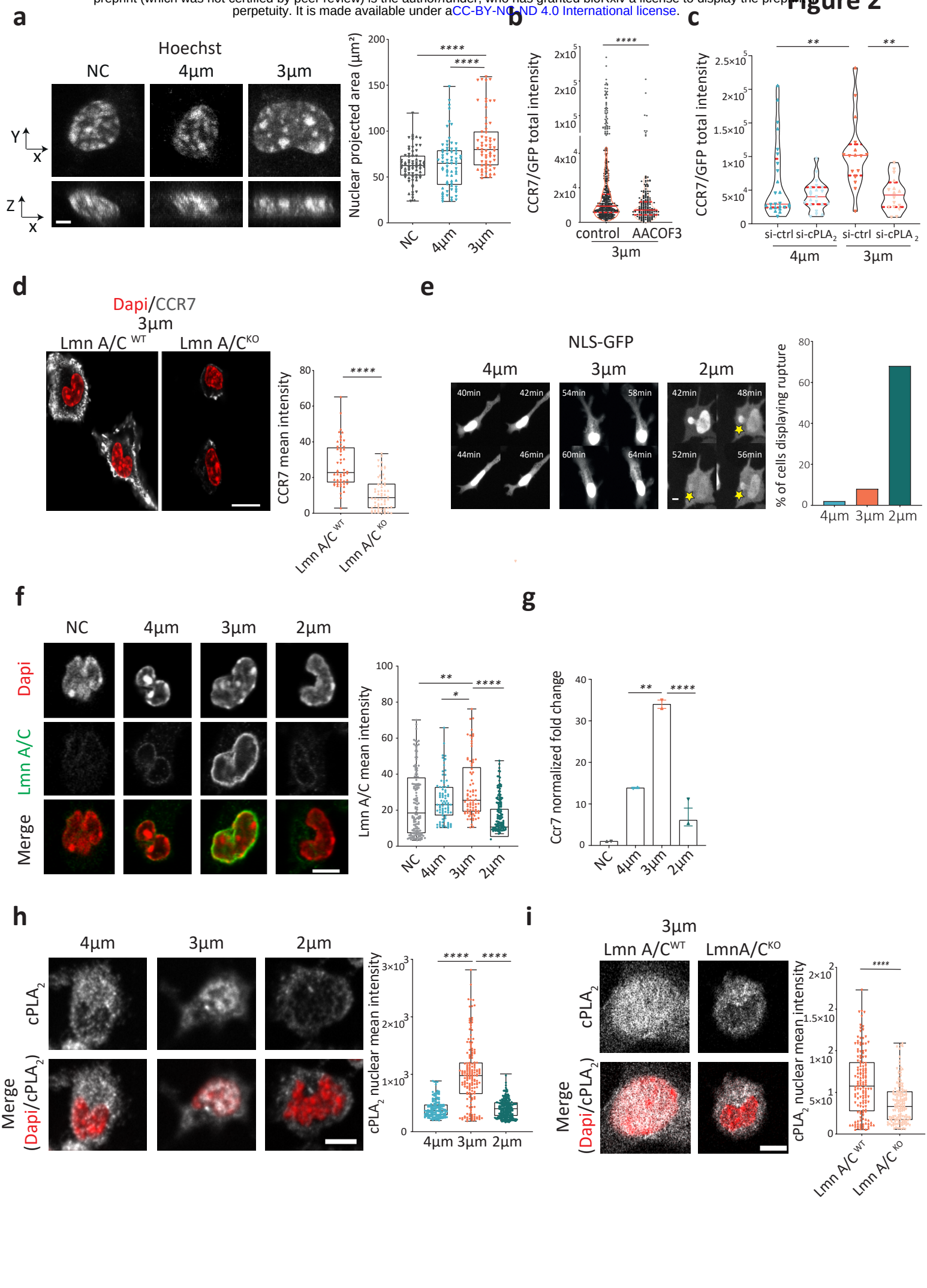

Figure 3

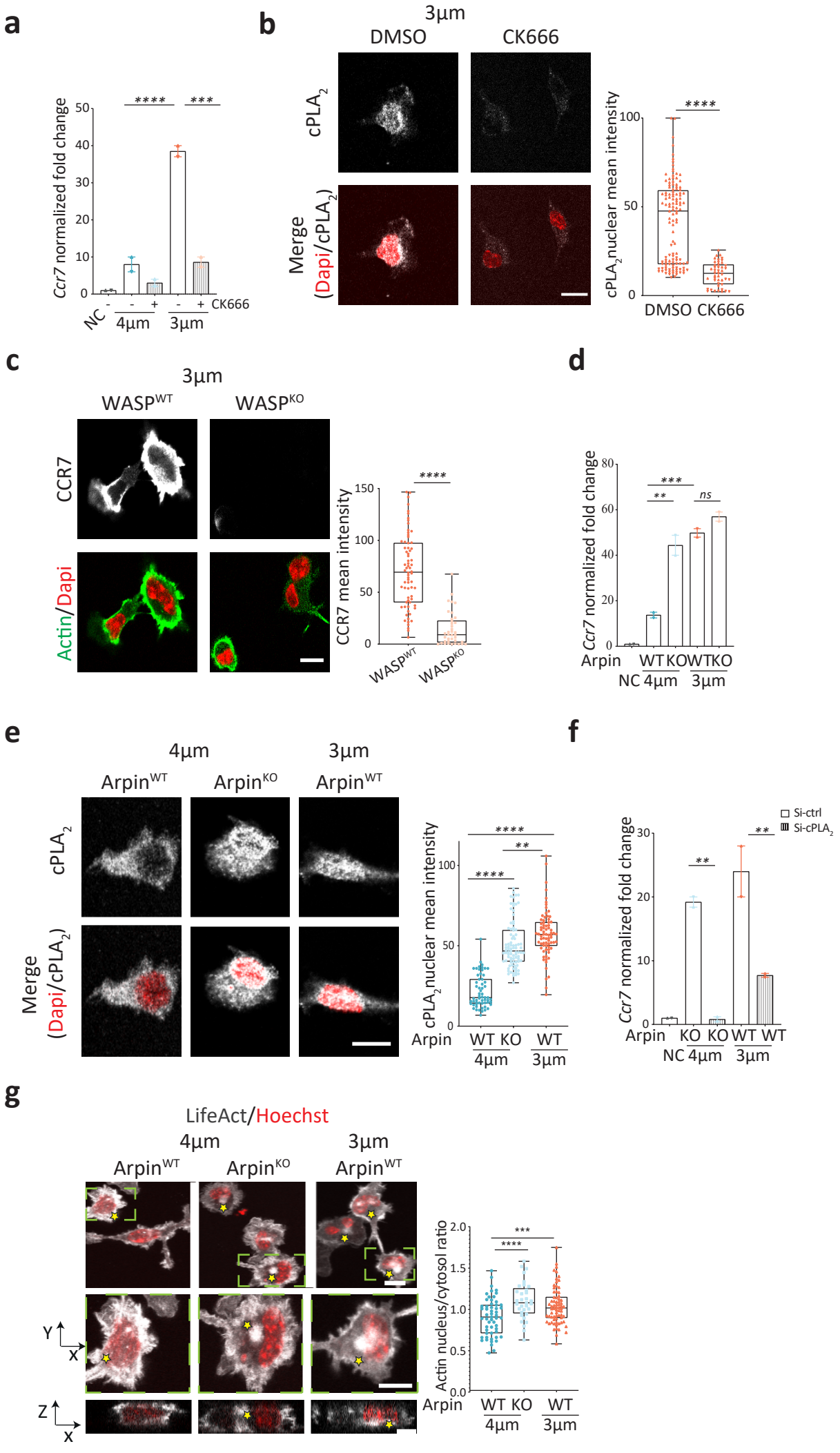

Figure 4

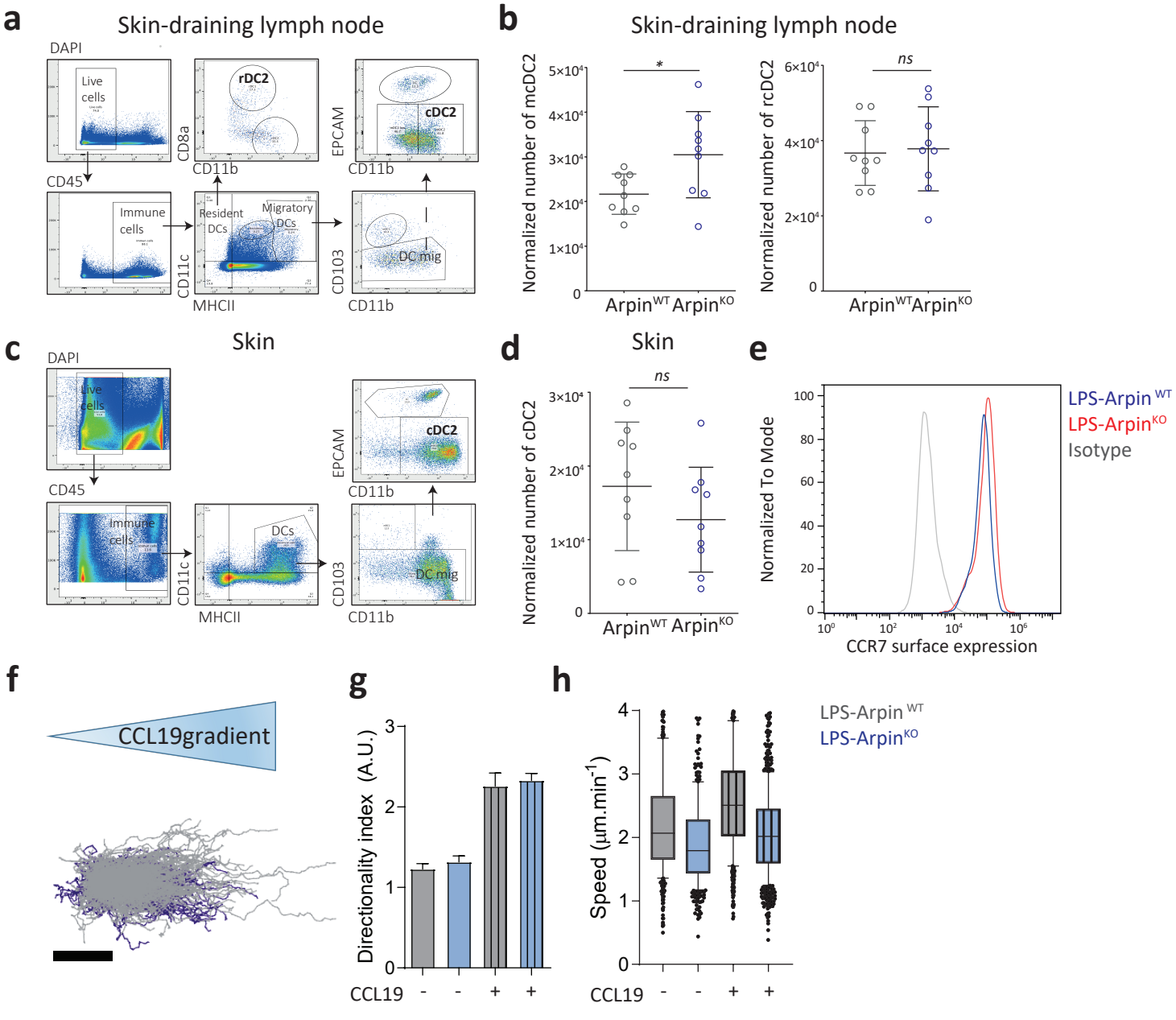

Figure 5

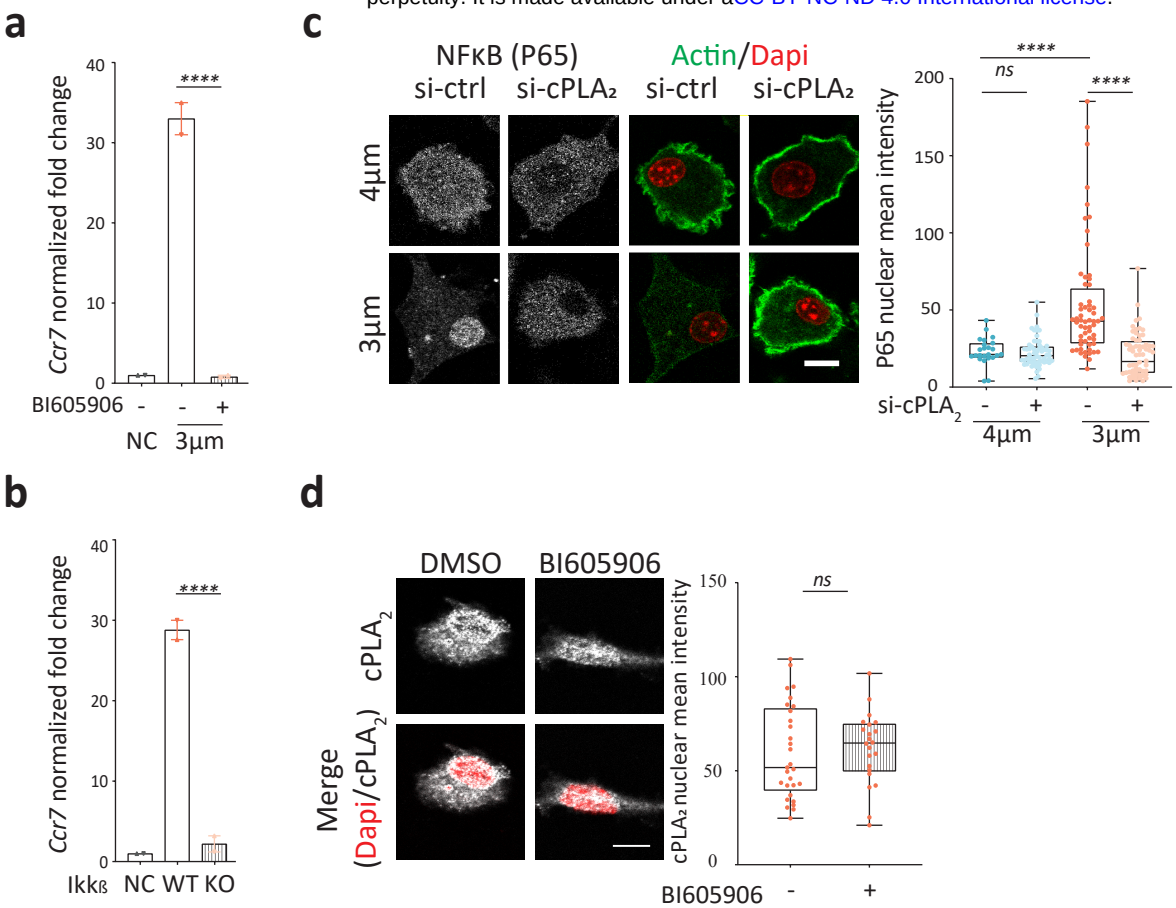

Figure 6

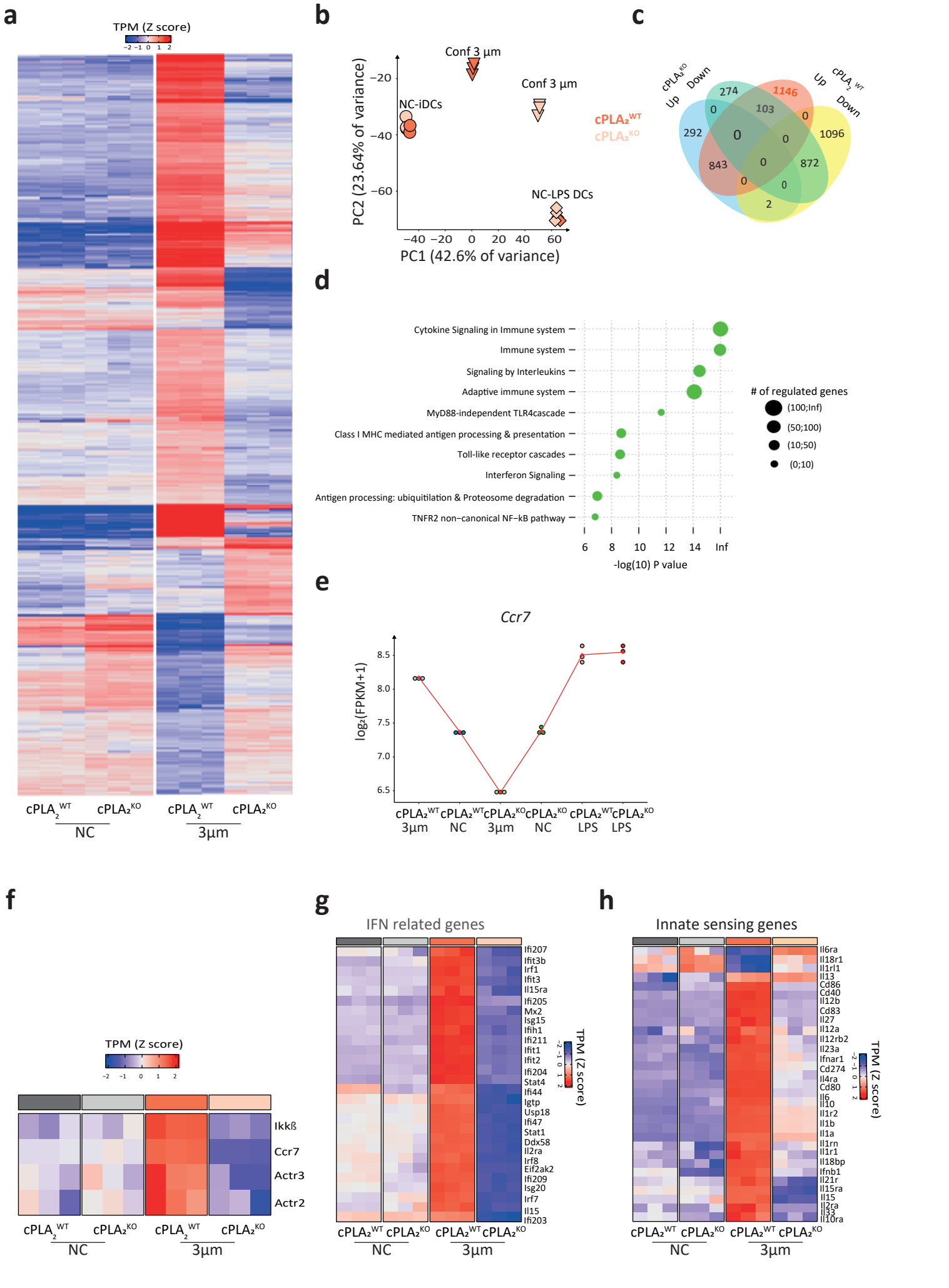

Figure 7

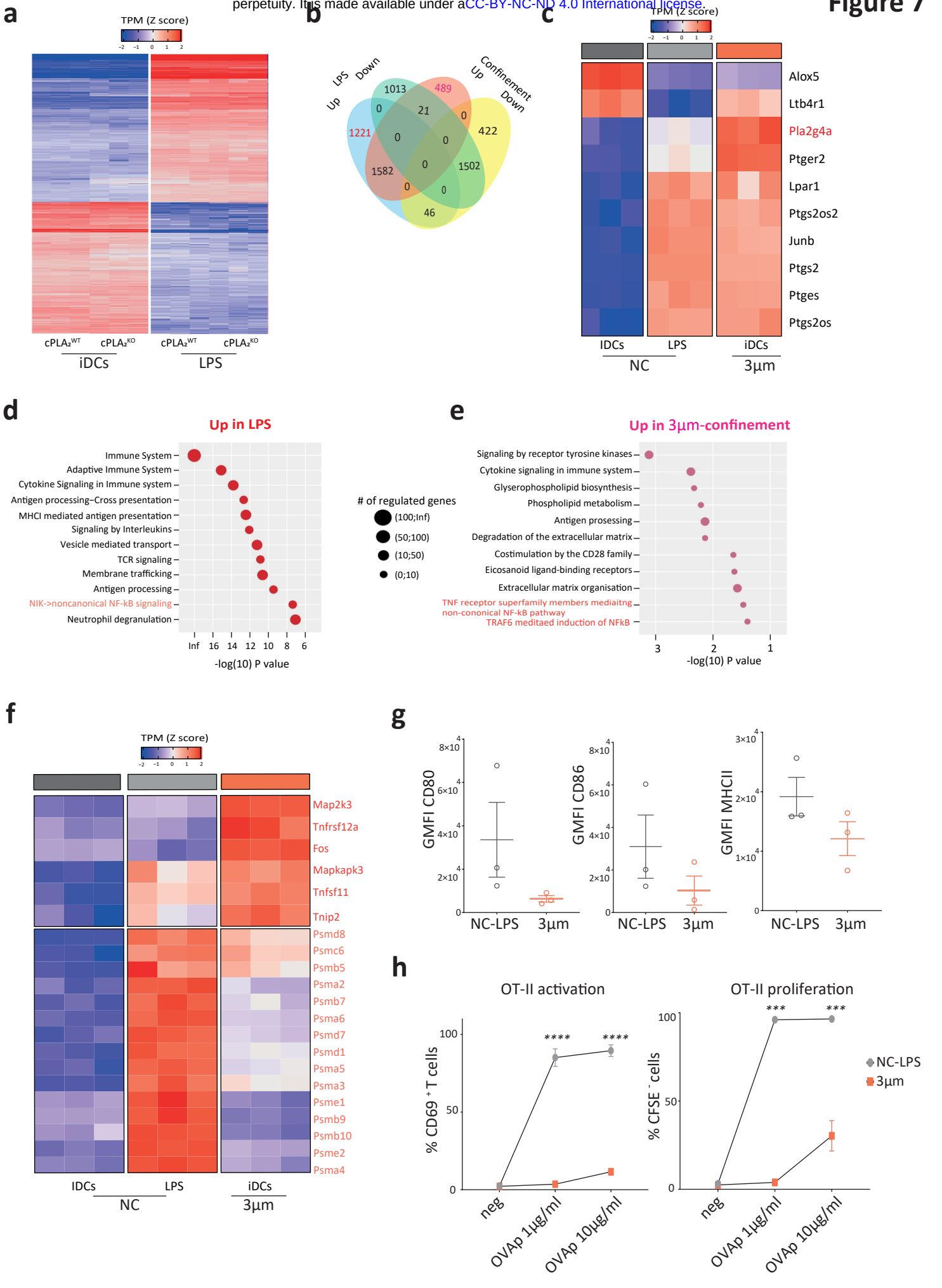

Figure S1

a

1. Choose the time point of interest
2. Draw each cell's outline and add to ROI manager
3. Measure the mean GFP intensity per cell
4. Total GFP Intensity = (mean intensity - median of the background)* cell area

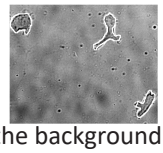

b

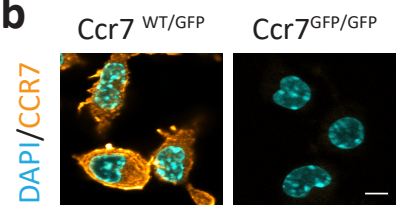

Figure S2

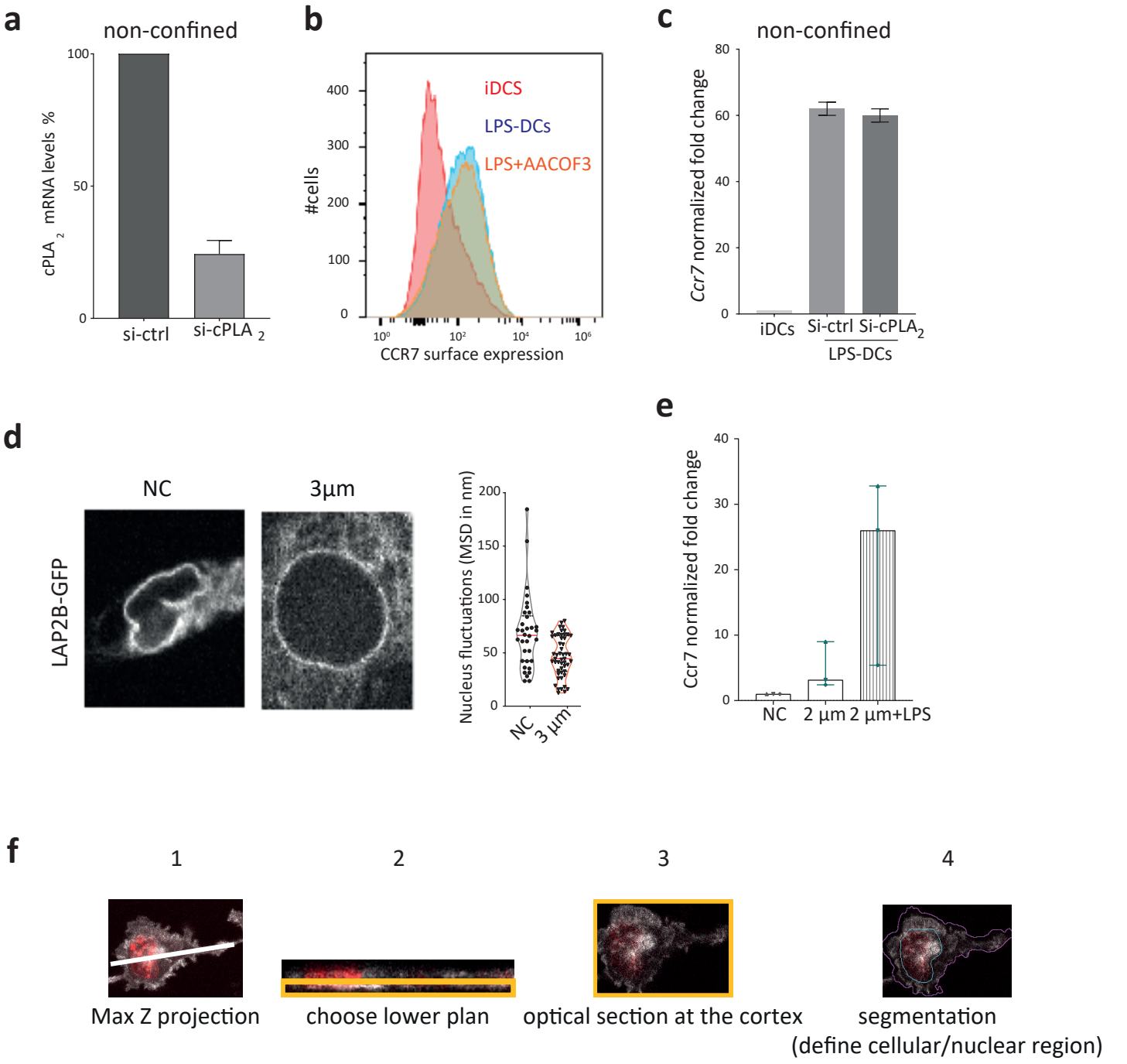

Figure S3